Draft version January 11, 2011
Preprint typeset using LaTeX style emulateapj v. 03/07/07

STAR FORMATION IN DISK GALAXIES. II. THE EFFECT OF STAR FORMATION AND PHOTOELECTRIC HEATING ON THE FORMATION AND EVOLUTION OF GIANT MOLECULAR CLOUDS

Elizabeth J. Tasker[1,2,3]

Draft version January 11, 2011

ABSTRACT

We investigate the effect of star formation and diffuse photoelectric heating on the properties of giant molecular clouds (GMCs) formed in high resolution ($\lesssim 10\,$pc) global ($\sim 20\,$kpc) simulations of isolated Milky Way-type galaxy disks. The clouds are formed through gravitational fragmentation and structures with densities $n_{\rm H,c} > 100\,{\rm cm}^{-3}$ are identified as GMCs. Between 1000-1500 clouds are created in the simulations with masses $M > 10^5\,{\rm M}_\odot$ and 180-240 with masses $M > 10^6\,{\rm M}_\odot$ in agreement with estimates of the Milky Way's population. We find that the effect of photoelectric heating is to suppress the fragmentation of the ISM, resulting in a filamentary structure in the warm gas surrounding clouds. This environment suppresses the formation of a retrograde rotating cloud population, with 88% of the clouds rotating prograde with respect to the galaxy after 300 Myr. The diffuse heating also reduces the initial star formation rate, slowing the conversation of gas into stars. We therefore conclude that the interstellar environment plays an important role in the GMCs evolution. Our clouds live between $0 - 20\,$Myr with a high infant mortality ($t' < 3\,$Myr) due to cloud mergers and star formation. Other properties, including distributions of mass, size and surface density agree well with observations. Collisions between our clouds are common, occurring at a rate of $\sim 1/4$ of the orbital period. It is not clear whether such collisions trigger or suppress star formation at our current resolution. Our star formation rate is a factor of 10 higher than observations in local galaxies. This is likely due to the absence of localized feedback in our models.

Subject headings: galaxies: spiral, galaxies: ISM, galaxies: star clusters, methods: numerical, ISM: structure, ISM: clouds, stars: formation

1. INTRODUCTION

Embedded in the turbulent gas of the interstellar medium (ISM) are the stellar nurseries of the Galaxy; the giant molecular clouds (GMCs). The properties of these clouds dictate the environment in which most new stars are formed, making these objects the primary controllers of star formation in the Galaxy. To understand star formation, it is therefore essential that we first understand the processes that govern the formation and evolution of the GMCs.

Exactly what determines the GMC properties is a taxing problem. Theoretical work on their formation has led to two different schools of thought. The "Top-down" mechanism suggests GMC formation is driven via large-scale gravitational or magnetic disk instabilities (e.g. Shetty & Ostriker 2006; Kim et al. 2003; Glover & Mac Low 2007a,b), whereas "bottom-up" processes see clouds formed in colliding flows (e.g. Heitsch et al. 2008) or via agglomeration from inelastic collisions between the GMCs (Kwan 1979). It is possible that both these processes are important in different galactic environments (Dobbs 2008).

Depending on the lifetime of the cloud, the importance of the formation mechanism on the GMC properties varies. If the cloud lives as long as a few free-fall times, then its attributes could depend primarily on interactions with its environment (e.g. disk sheer, spiral arms and cloud-cloud collisions), and also on its internal processes driven by star formation, including turbulence from supernovae and radiation pressure. Whether GMCs are long-lived enough for this is highly debated with theories supporting lifetimes both short and long compared to the free-fall timescale,

$$t_{ff} = \left(\frac{3\pi}{32G\rho}\right)^{1/2} = 4.35\times 10^6 \left(\frac{n_{\rm H}}{100{\rm cm}^{-3}}\right)^{-1/2} {\rm yr}. \quad (1)$$

However, current estimates suggest that a GMC lives between 1-2 free-fall times (e.g. McKee & Ostriker 2007, and references therein). This implies that the cloud's evolution could play a significant role in determining its properties.

Observationally, it is difficult to measure the cloud properties accurately since the molecular gas cannot be measured directly, but must be inferred from the abundances of CO (Glover et al. 2010; Shetty et al. 2010). From the theoretical stand point, there is the problem of scale that the forces are operating on. While the GMC itself is of order 20 pc in radius, it lives in a galactic disk whose stellar component, in the Milky Way, extends to around 20 kpc in radius. This means to self-consistently replicate their properties, simulations of GMCs must encompass 3-4 orders of magnitude in scale. Previous work that has studied the properties of GMCs on the galactic scale has often been limited to two dimensions (Shetty & Ostriker 2008) or has had to assume a fixed two-phase medium for the ISM (Dobbs 2008). While the majority of the clouds are confined to the plane of the disk, both cloud collisions and feedback eject gas from the surface and, in the latter instance,

[1] CITA National Fellow
[2] Department of Physics and Astronomy, McMaster University, 1280 Main Street West, Hamilton, Ontario L8S 4M1, Canada.
[3] Department of Astronomy, University of Florida, Gainesville, FL 32611, USA

it is this vertical expulsion that is thought to regulate the pressure in the ISM (McKee & Ostriker 1977; Cox 2005); the environment in which the clouds are forming. Similarly, previous three dimensional studies of the ISM in galaxy disks at lower resolution, produce a continuous multiphase medium that is poorly represented by a fixed, discrete phase model (Tasker & Bryan 2006, 2008; Wada & Norman 2007).

Local models which consider a partial region of the galaxy disk (normally less than a few kpc across) are able to achieve much higher resolutions and –with the use of a shearing box– can approximate the effects of galactic shear on the cloud properties (Kim et al. 2008; Kim & Ostriker 2007, 2006, 2001). Alternative models on similar scales investigate the results from colliding flows (Heitsch et al. 2008, 2009) and the local impact of supernovae and turbulence (e.g. Joung & Mac Low 2006; Slyz et al. 2005). These simulations are able to tell us much about the structure of the GMCs and star-forming gas, but they cannot explore the evolution of the GMCs as they move through the disk or compare with globally averaged properties.

Whether the global environment is important for correctly modeling the evolution of the GMCs remains an open question. If GMC properties are not a strong function of their environment, then they can be modeled as separate entities and the inclusion of global forces from the galactic disk are not necessary. This hypothesis is given some support by the observational results from populations of GMCs in galaxies other than the Milky Way, which find their properties are similar to those of Galactic GMCs, including their velocity dispersions, surface density and virial parameters (Bolatto et al. 2008; Rosolowsky et al. 2003; Fukui et al. 2008). Bigiel et al. (2008) also found that the 18 galaxies in The HI Nearby Galaxy Survey (THINGS) appeared to have a fixed star formation rate (SFR) per unit of molecular gas, all of which could suggest a set of universal properties for GMCs.

On the other hand, if the clouds are gravitationally bound, then their velocity dispersions become established via GMC interactions (Gammie et al. 1991). In this case, their radial position in the galaxy can change, causing greater susceptibility to galactic shear. Both Gammie et al. (1991) and Tan (2000) argue that self-gravitating GMCs should suffer relatively frequent collisions, which could be an important process in controlling the molecular mass of a GMC. This would impact the GMC's SFR, making the galactic environment an essential ingredient in the GMC's evolution. Furthermore, while the mass profile of GMCs is universally seen to be a power law of the form,

$$\frac{dN_c}{d\ln M_c} \propto M_c^{-\alpha_c}, \tag{2}$$

the value of the exponent, α_c, is found to differ between galaxies. Williams & McKee (1997) measure a value of α_c between $0.6 - 0.8$ in the Milky Way, while Rosolowsky et al. (2003) finds a steeper gradient of $\alpha_c \simeq 1.6$ in M33. Blitz & Rosolowsky (2004) conclude that these variations are not due to systematic uncertainties, but are a consequence of the galactic environment. This suggests that the global-scale structures impact the range of masses of clouds formed.

Perhaps most suggestive evidence in favor of an intrinsic connection between clouds and their galactic environment is the Kennicutt-Schmidt relation (Kennicutt 1998). This empirical relation links the averaged gas surface density, $\bar{\Sigma}_{\rm gas}$ to the surface density of star formation rate $\bar{\Sigma}_{\rm sfr}$ via:

$$\bar{\Sigma}_{\rm sfr} \propto \bar{\Sigma}_{\rm g}^{\alpha_{\rm sfr}} \tag{3}$$

where Kennicutt (1998) found the exponent $\alpha_{\rm sfr} = 1.4 \pm 0.15$ for spatial averaging over the entire disk. More recent studies using the THINGS data (Bigiel et al. 2008) find the relation to hold linearly with the molecular component of the gas with a $\alpha_{\rm sfr} = 1.0 \pm 0.2$, with spatial averaging (resolution) of 750 pc.

An alternatively fit for this data can be found by relating $\bar{\Sigma}_{\rm sfr}$ to the orbital angular frequency at the outer radius, $\Omega_{\rm out}$: $\bar{\Sigma}_{\rm sfr} \propto \bar{\Sigma}_g \Omega_{\rm out}$. This result applies even in the more extreme environments of starburst and high red-shift galaxies (Genzel et al. 2010). Both these relations indicate an intimate connection between global structure and the GMC star-forming environment.

On scales of the same order as the GMC size, an important component in the GMC evolution must come from the stars themselves. Star formation is observed to be highly clustered, with star clusters forming out of dense clumps with initial radii ~ 1 pc (Lada & Lada 2003). Within this small region, the total star formation efficiency is relatively high at $\sim 0.1 - 0.5$, but the majority of the GMC is not forming stars, possibly due to the effect of magnetic fields (Crutcher 2005). The average efficiency over the whole cloud is therefore of order a few percent per local free-fall time (Krumholz & Tan 2007; Zuckerman & Evans 1974).

Gas is removed from the cloud to create a star which then deposits energy into its surrounding medium through diffusive and energetic feedback. During its lifetime, a massive star will be source of FUV radiation which can be absorbed by dust grains to eject an electron that will heat the gas. This photoelectric heating has long been thought to be the dominant form of heating in the neutral ISM, which includes the GMC population (Wolfire et al. 1995). More energetic forms of feedback from stellar winds and supernovae will also act to deposit concentrated blasts of energy into the star's immediate environment. Whether the cloud can survive the star's life-cycle is debated (e.g. Murray 2010) but the fact this process will affect the cloud's properties is not.

Due to the range of the forces in play, it is exceptionally difficult to determine the dominant processes affecting a GMC's evolution. Is it the interaction with the global galaxy environment, the results of star formation and feedback or an equal combination of systems? In these papers, we aim to investigate this with a set of global disk simulations that separate out the processes by introducing each influencing factor individually.

In our first paper (Tasker & Tan 2009, hereafter TT09), we simulated an idealized population of GMCs without the presence of star formation or any form of feedback. Despite the simplicity of the model, we reproduced many of the observable properties of measured GMC populations including mass surface density, velocity dispersion, angular momentum and vertical distribu-

tion. In addition to this, we found a typical collision time between clouds of $\sim 20\,\%$ of the local orbital time, in agreement with estimates by Tan (2000). This suggested that compressive flows generated in cloud collisions could be a dominant mechanism for inducing star formation. Such a process has parallels with the local-scale colliding flow models which trigger star formation via compressive forcing of the turbulent flows (Banerjee et al. 2009; Heitsch et al. 2008; Hennebelle et al. 2008). However, for this simulation without star formation and feedback processes included in the model, the GMCs could only be destroyed through mergers. This meant that it was not possible to regulate their evolution, giving a steadily more massive population over time.

In this paper, we extend the model in two new simulations. The first of these includes star formation without feedback and the second contains star formation with diffuse feedback from FUV photoelectric heating. We compare the properties of the GMC populations formed in both models and with the GMCs formed without star formation in TT09. Our results will show that the diffuse heating reduces the fragmentation of the disk, causing clouds to be embedded in a filamentary warm ISM. This reduces the initial star formation rate and suppresses the formation of a retrograde rotating population of clouds. We will see that both our population of clouds continue to match many of the observations of GMCs in the Milky Way, including the mass profile, size, mass weighted surface density, vertical distribution and gravitational binding. With the inclusion of cloud destruction through star formation and mergers, we are able to estimate the average lifetimes of the clouds in our populations which are found to be largely between $0-20\,$Myr in agreement with current estimates. We will show that our SFR is a factor of 10 higher than that observed in local galaxies and suggest that this is due to the lack of energetic local feedback in our models.

These localized feedback processes, such as supernovae, radiation pressure and ionization are expected to play an important role in GMC evolution. However, to understand the determining forces on the GMC population, we focus on the two effects of star formation and diffuse heating in this paper, leaving additional forces for later study.

Details of our method are outlined in section §2, global properties of the disk are presented in §3 and the structure of the ISM in §4. §5 will focus on the properties of the individual GMCs and §6 will look at the star formation in the disk. In §7 we will present our conclusions.

2. NUMERICAL TECHNIQUES

2.1. *The Code*

The simulations presented in this paper were run using *Enzo*; a three-dimensional adaptive mesh refinement (AMR) hydrodynamics code (O'Shea et al. 2004; Bryan 1999; Bryan & Norman 1997). The AMR technique is particularly adept at resolving multiphase fluids such as those found in the ISM, due to the natural boundaries between grid cells producing accurate resolution of shocks and low numerical mixing (Tasker et al. 2008). *Enzo* has previously been used to model galactic disks where it successfully produced a self-consistent atomic multiphase ISM (Tonnesen & Bryan 2010; Tasker & Tan 2009; Tasker & Bryan 2008, 2006).

We used a three-dimensional box of side 32 kpc with a root grid of 256^3 and four levels of refinement, giving a limiting resolution (smallest cell size) of 7.8 pc. For the effect of resolution on our simulation results, see TT09 where a detailed study is presented. Gas was refined whenever the Jeans' Length was resolved by less than four cell widths, as suggested by Truelove et al. (1997) as the resolution needed for avoiding artificial fragmentation. On our finest level, the Truelove criteria is maintained until $\sim 100\,\mathrm{cm}^{-3}$, our threshold density for cloud definition. A discussion on resolving the gravitational collapse in the simulation is presented more fully in TT09.

The evolution of the gas in *Enzo* was performed using a three-dimensional version of the *Zeus* hydrodynamics algorithm (Stone & Norman 1992). This routine uses an artificial viscosity term to represent shocks, where the variable associated with this, the quadratic artificial viscosity, was set to 2.0 (the default) for all simulations.

Radiative cooling was included using rates from the analytical expression of Sarazin & White (1987) for solar metallicity to $10^4\,$K and down to $T = 300\,K$ using rates from Rosen & Bregman (1995). This allows the gas to cool to the temperature of the upper end of the atomic cold neutral medium (Wolfire et al. 2003). Actual GMCs will have temperatures of $\sim 10\,$K, an order of magnitude below our minimum temperature. However, at our resolution, clouds with diameters of 100 pc only have 13 cells in each linear dimension (with an average GMC having a radius of 16 kpc and 4 cells across), which is insufficient to resolve the full turbulent structure of the gas. We also do not include pressure from magnetic fields, so imposing this temperature floor of 300 K produces a minimum sound speed of $1.8\,\mathrm{kms}^{-1}$ to crudely allow for these effects. In fact, the velocity dispersion within our clouds is typically higher than this by about a factor of two, implying that this floor is not having a significant impact on our cloud properties.

In addition to radiative cooling, the gas can also be heated via diffuse photoelectric heating in which electrons are ejected from dust grains via FUV photos. In the simulation where this was turned on, we included a radially dependent heating term of the form described in Wolfire et al. (2003):

$$\Gamma_{\mathrm{pe}} = 10^{-24}\epsilon_h G_0 \begin{cases} e^{-(R-R_0)/H_R}\,\mathrm{ergs\,s}^{-1} & \mathrm{r} \geq 4.0\,\mathrm{kpc} \\ e^{-(4-R_0)/H_R}\,\mathrm{ergs\,s}^{-1} & \mathrm{r} < 4.0\,\mathrm{kpc} \end{cases} \tag{4}$$

where the heating efficiency $\epsilon_h = 0.05$ and G_0 is the incident far-ultraviolet field normalized to the Habing (1968) estimate for the local ISM value. We take a value of $G_0 = 1.7$ in agreement with Draine (1978). R_0 is the radial scale length at 8.0 kpc and $H_R = 4.1\,$kpc, the scale length as estimated by Wolfire et al. (2003).

Collisionless star particles, representing star clusters, are allowed to form in our simulation in the main region of the disk between $2.5 < r < 8.5\,$kpc. As is described in 2.2 below, this is the area of our disk where we identify and analyze the GMCs. Within this region, star parti-

cles are created when the density within a cell exceeds the threshold value of $n_{\rm H} = 100\,{\rm cm}^{-3}$. Since our finest refinement cells (where the stars will be formed) are still 7.8 pc across, the gas within them can be assumed to be turbulent. We therefore do not check for gravitational collapse or boundedness of the cell gas, since such processes are likely to affect star formation on much smaller scales than what we can resolve. Cells with temperatures greater than 3000 K are also prevented from forming stars to rule out the possibility of star formation in the hot dense gas of shock fronts. In practice, star particles form in gas typically close to 300 K, so this limit is not particularly important. When a cell reaches the threshold density, a star particle is created whose mass is calculated by:

$$m_* = \epsilon_{\rm ff}\frac{\Delta t}{t_{\rm ff}}\rho_{\rm gas}\Delta x^3 \tag{5}$$

where ϵ is the star formation efficiency (the fraction of gas that is converted into star particles per dynamical time), Δt is the size of the time step, $t_{\rm ff}$ is the time for dynamical collapse in the cell ($t_{\rm ff} = \left(\frac{3\pi}{32G\rho}\right)^{1/2}$) and $\rho_{\rm gas}$ is the gas density. The resultant object should be considered a star cluster, rather than an individual star since it contains approximately $1000\,{\rm M}_\odot$. For our simulations, we chose a value for $\epsilon_{\rm ff} = 0.02$, in agreement with the observational constraints described by Zuckerman & Evans (1974) for GMCs and Krumholz & McKee (2005) for GMCs and their internal, higher density components.

An additional computational requirement is that the star particle will not be created if the calculated value for m_* is less than a given minimum value of ${\rm m_{min}} = 10^3\,{\rm M}_\odot$. This purely numerical addition is to prevent the calculation becoming prohibitively slow due to a extremely large number of star particles. In the situation where this occurs, an override exists whereby a particle of mass $m_{\rm min}$ is created with a probability equal to the ratio between the mass of the would-be star particle and $m_{\rm min}$. In practice, almost all star particles born in the highest resolution simulations are created via this stochastic method with masses equal to $m_{\rm min}$.

The motions of the star particles are calculated as a collisionless N-body system. They interact gravitationally with the gas via a cloud-in-cell mapping of their positions onto the grid to produce a discretized density field. The number of star particles created during the simulations is 2.5 - 3 million. In this paper, there is no localized feedback to the gas directly from the star particle.

2.1.1. *Runs Performed*

This paper presents the results from two different simulations, both at a limiting resolution of 7.8 pc.

The first simulation (simulation *disk SFOnly*) includes star formation, implemented as described above, but with no form of additional heating. The second simulation (simulation *disk SF+PEheat*) also includes star formation and a radially dependent diffuse heating term with the form given by Equation 4.

The results in the absence of both star formation and diffuse heating are presented in TT09, simulation *disk NoSF*.

2.2. *Galaxy Initial Conditions and Cloud Analysis*

The initial conditions for the simulations are described in detail in TT09. They consist of an isolated gas disk sitting in a static background potential that represents both a dark matter halo and a stellar disk component for a galaxy similar to the Milky Way. The potential gives the disk a constant circular velocity for $r >> 0.5$ kpc of $v_c = 200\,{\rm km\,s^{-1}}$.

We focus on the gas in the main region of the disk between $2.0 < r < 10.0$ kpc. Gas here is initially marginally stable against gravitational collapse, with the Toomre Q parameter for gravitational instability (Toomre 1964) having a constant value:

$$Q = \frac{\kappa\sigma_g}{\pi G\Sigma_g} \sim 1.5 \tag{6}$$

where κ is the epicycle frequency and Σ_g, the gas surface density. $\sigma_g \equiv \sqrt{\sigma_{nt}^2 + c_s^2}$ is the mass-weighted 1D velocity dispersion of the gas, with σ_{nt} being the velocity motions in the disk plane after subtraction of the circular velocity. The vertical profile is proportional to ${\rm sech}^2(z/z_h)$, where the scale height, z_h varies with galactocentric radius based on HI observations of the Milky Way (Binney & Merrifield 1998). At the solar radius of 8 kpc, $z_h = 290$ pc. For a flat rotation curve, $\kappa = \sqrt{2}v_c/r$, which gives a gas density profile of the form:

$$\rho(r,z) = \left(\frac{\sqrt{2}v_c\sigma_g}{4\pi GQz_h}\right)\frac{1}{r}{\rm sech}^2\left(\frac{z}{z_h}\right)$$

Low density regions of gravitationally stable gas sit in the disk center between $0 < r < 2$ kpc and at the outer edge between $10 < r < 12$ kpc.

As the gas cools, the main region of the disk becomes gravitationally unstable with $Q < 1$ and fragments. Star formation and cloud analysis are restricted to between $2.5 > r > 8.5$ kpc; within the main region but avoiding boundary effects.

Details of the algorithm used to identify and track the GMCs in the simulations are described in TT09. In short, we identify "GMCs", i.e. star-forming clouds, as peaked and coherent structures contained within contours of the threshold density of $n_{\rm H,c} \geq 100\,{\rm cm}^{-3}$, about the mean volume density of observed galactic GMCs. It is worth remembering that while GMCs are by definition molecular, our gas is purely atomic, so we are selecting structures that would be mostly molecular in reality, although our procedure does not distinguish dense atomic gas that might be present in photodissociation regions. By comparing outputs of the simulation at 1 Myr intervals, the clouds are tracked over the course of the simulation to produce a timeline of their evolution. The simulations themselves are run for 300 Myr, just over one orbital period at the outer edge of the main region in the disk.

3. GLOBAL EVOLUTION OF THE GALACTIC DISK

The disk rapidly cools from its initial conditions to fragment through gravitational instabilities (see TT09 for a discussion of this process). By $t = 140$ Myr, the main region of the disk between $2.5 > r > 8.5$ kpc has

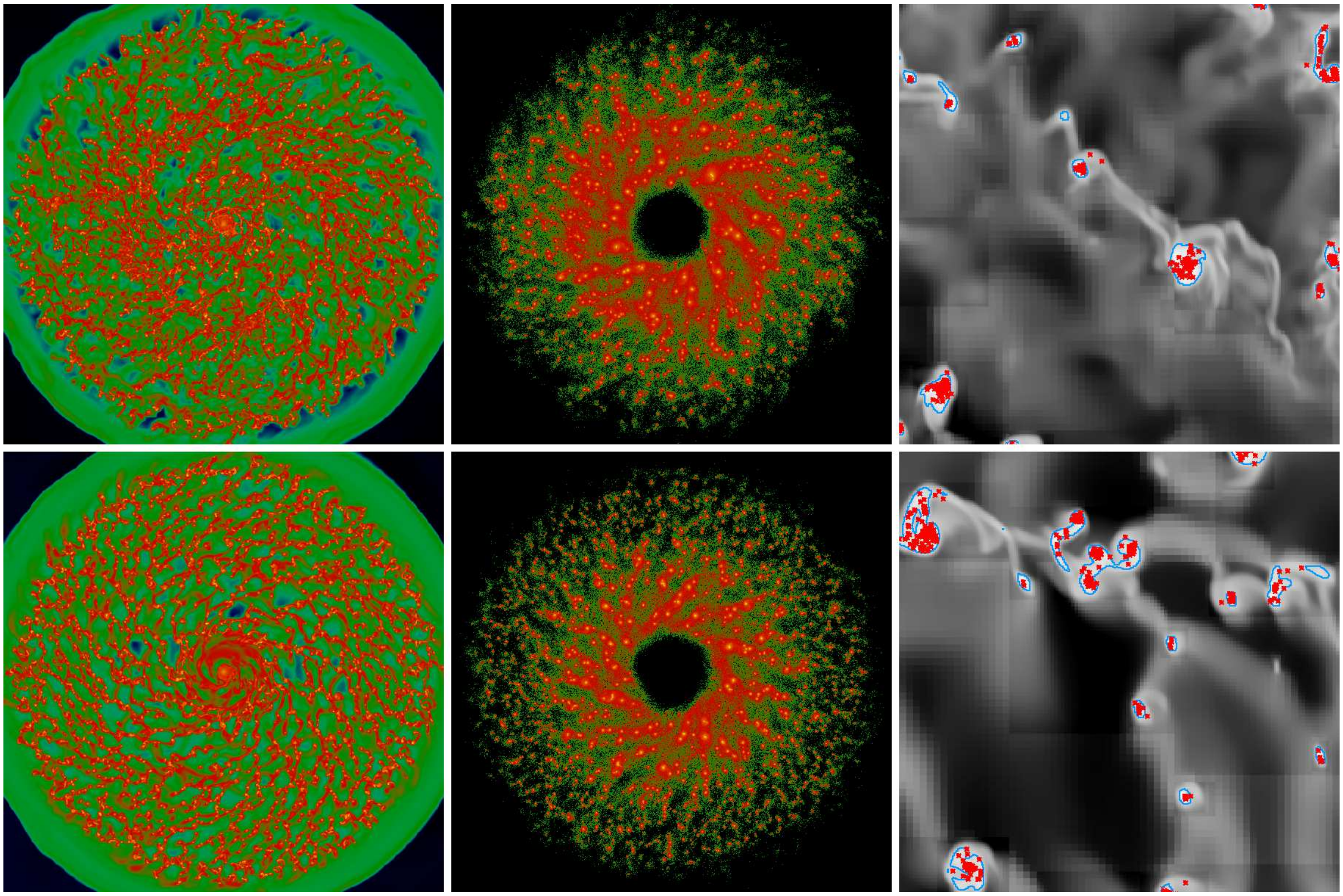

FIG. 1.— Images of the galactic disk at 200 Myr. Top panel is for disk SFOnly while the bottom panel shows disk SF+PEheat. The left-hand image is 20 kpc across and shows the log-scaled surface density of the disk with range $[0.0033, 3715]\,\mathrm{M_\odot}pc^{-2}$. The center pane is the projected star particle density and the right-hand image shows a 2 kpc density slice of the mid-plane. Blue contour lines mark the cloud boundaries corresponding to a number density of $100\,\mathrm{cm}^{-3}$ and the new star particles (age < 1 Myr) are shown in red.

fully fragmented into dense cold clouds of gas, embedded in a warmer medium.

Three images of the disk at $t = 200$ Myr are shown in Figure 1 for simulation disk SFOnly (top row) and disk SF+PEheat (bottom row), where diffuse heating is included. The left-hand panel shows the gas surface density over the main region of the disk, the middle panel shows the star particle density for the same region and the right-hand panel displays a 2 kpc slice of a typical patch in the galactic mid-plane. In this right-hand panel, blue contours mark our cloud threshold definition of $100\,\mathrm{cm}^{-3}$ and new star particles, with age < 1 Myr, are shown in red.

The effect of including the diffuse heating on the disk's ISM can be seen in the images of the gas surface density. Without the additional heating in disk SFOnly, the gas collapses to form smaller structures, especially in the inner region, $2 > r > 4$, where both the density of the disk is highest (and hence the dynamical time shortest) and the heating term, as described in equation 4, is at its maximum. While the disk has evidently become gravitationally unstable in both cases, its fragmentation is reduced by the diffuse heating.

One of the main results of the reduced fragmentation is shown in the middle panel of Figure 1 in the distribution of star particles. The stellar density is visibly lower when diffuse heating is included. At $t = 200$ Myr, disk SFOnly has formed over 3 million star particles, whereas this is reduced to 2.6 million in disk SF+PEheat. The star formation properties of the disk will be considered quantitatively in section 6.

The findings from the first two image panes in Figure 1 are supported in the close-up of the 2 kpc slice of the galactic plane on the far-right. The filaments connecting sites of star formation are denser and thicker in disk SF+PEheat and the smaller star formation regions appear to have less stars within them than ones of similar diameter in disk SFOnly.

The new star particles are born inside the identified cloud boundaries, as expected since the density threshold for both cloud identification and star formation is $n_{\mathrm{H,c}} = 100\,\mathrm{cm}^{-3}$. In the occasional case where a star particle appears to exist just outside the cloud boundary, it has either moved during the last 1 Myr or destroyed (via mass removal) the small part of its cloud that it was formed in. With diffuse heating, the gas between the clouds forms thicker filaments, supported against further fragmentation by the thermal addition. This gives the warm ISM between the clouds a more coherent structure.

This variation in the global structure of the disk, together with its evolution, is shown quantitatively in Figure 2. The four plots show azimuthally averaged radial profiles of the disk properties for disk SFOnly (top row)

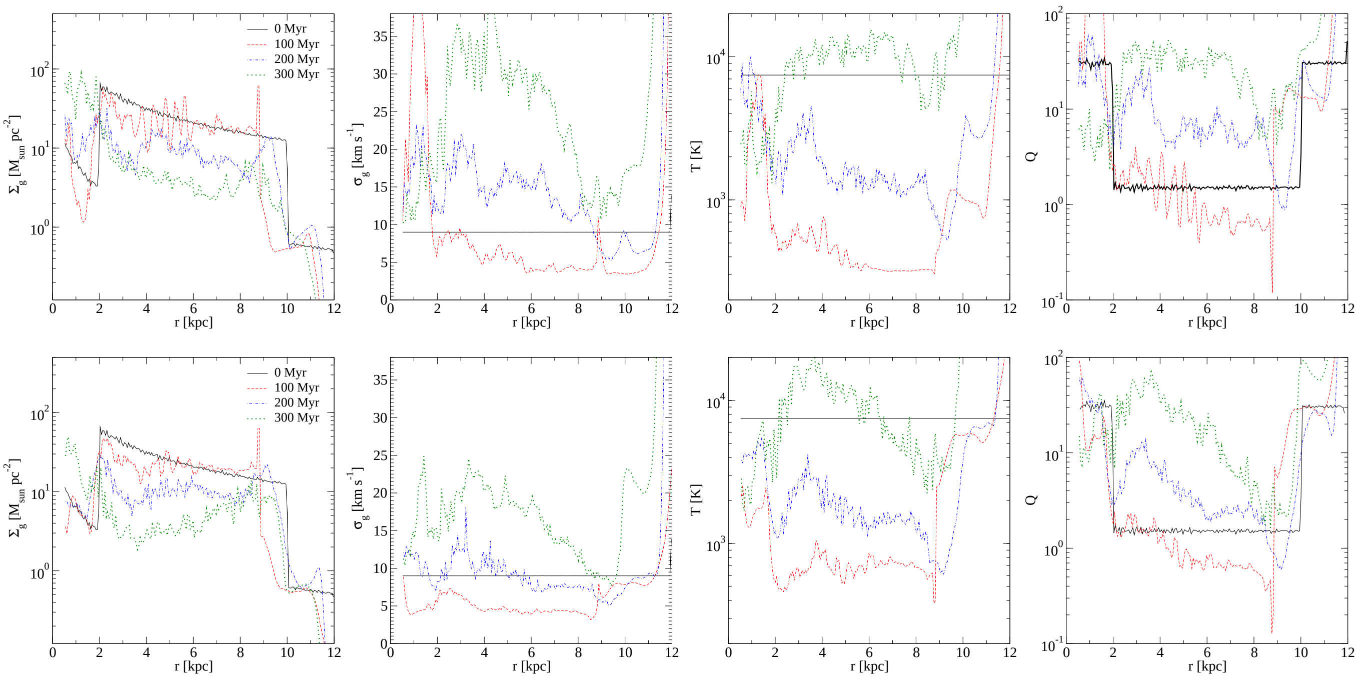

FIG. 2.— Evolution of the azimuthally-averaged radial galactic profiles for disk SFOnly (top row) and disk SF+PEheat which (bottom row). Plots left to right show: (a) gas mass surface density (Σ_g), (b) 1D velocity dispersion of the gas (σ_g), (c) temperature (T) and (d) Toomre Q parameter. Note, $\Sigma_g = \int_{-1\mathrm{kpc}}^{+1\mathrm{kpc}} \rho(z)dz$, T is a mass-weighted average over -1 kpc $< z <$ 1 kpc and Q makes use of σ_g evaluated as a mass-weighted average over the same volume.

and disk SF+PEheat (bottom). From left to right, the plots are: (1) gas surface density, $\Sigma_g = \int_{-1\,kpc}^{+1\,kpc} \rho(z)dz$, (2) the gas velocity dispersion, σ_g, calculated via a mass-weighted average over $-1\,\mathrm{kpc} < z < 1\,\mathrm{kpc}$ utilizing only disk plane velocity components, (3) the mass-weighted temperature, T, averaged over the same range as σ_g and (4) the Toomre Q parameter for gravitational instability as given in Equation 6. The four lines on each plot show the profile at different times (t = 0, 100, 200 and 300 Myr) during the simulation.

The initial conditions at $t = 0$ are shown by the black solid line in all plots. We can see our main disk region between $2.5 < r < 8.5$ kpc is initially at a surface density higher than the surrounding gas by over an order of magnitude and has a constant borderline stable $Q = 1.5$. The initial temperature is constant over the entire simulation box and corresponds to a sound speed of $c_s = 9\,\mathrm{km s^{-1}}$.

During the first 100 Myr (red dashed line) the gas cools, bringing Q below the critical stability value of 1.0 and causing the gas to fragment. In the top panel showing disk SFOnly, the temperature drops until it approaches the floor of our radiative cooling curve at 300 K, whereas the addition of diffuse heating in the bottom panel slows down the cooling of the densest clumps, increases the average minimum temperature reached by approximately a factor of 2.0. Global ring instabilities appear in the surface density profiles of both simulations (see TT09 for images of their formation), but are less prominent in the gas warmed by the diffuse heating, which provides an extra thermal support. As the disk fragments tangentially, these fluctuations flatten out. The magnitude of the surface density remains almost constant over the disk's main region during this early period. At lower radii, however, the circular motion becomes poorly resolved by the Cartesian grid, causing an infall of low density gas from the inner region of the disk to build up at the disk center.

By the time the simulation reaches 200 Myr (blue dot-dashed line), star formation has depleted the gas, causing the surface density to drop by a factor of 2.0 in disk SFOnly and 1.5 for disk SF+PEheat. Since star formation occurs in the coldest and densest regions of the disk, the azimuthally averaged temperature rises as do the corresponding values for the velocity dispersion and Q. The velocity dispersion also increases due to gravitational heating, as star particles are formed to create local deep potential wells. This effect is strongest in the disk without diffuse heating, since 500,000 more star particles have formed by this time, causing a greater depletion of the dense gas.

Star formation continues to deplete the gas, resulting in the surface density dropping by a factor of about 6 from the initial conditions by 300 Myr at $r = 6$ kpc for both runs (green dotted line). The SFR is highest in the densest gas (since it is proportional to the free-fall time), causing the surface density to drop first in the inner part of our main region, $2.5 < r < 4$ kpc. This is marked most in disk SF+PEheat, where the star formation progresses more slowly due to the reduced fragmentation.

The velocity dispersion is significantly lower in disk SF+PEheat, having increased more slowly over the 300 Myr. This initially seems surprising, since the temperature is higher, but diffuse heating has reduced the ability of the disk to fragment into massive bound clusters, as was seen in Figure 1, leaving a filamentary state that reduces the in-plane velocity motions, σ_{nt}, (and the corresponding Q value), that are excited by gravitational

interactions between fragmented clumps.

4. THE STRUCTURE OF THE ISM

A one dimensional analysis of the structure of the ISM in the main region of the disk can be seen in the probability distribution functions (PDFs) plotted in Figure 3 for the simulations at the same times shown in Figure 2. The top two graphs show the gas volume fraction as a function of density for the disk SFOnly (left) and for disk SF+PEheat (right). The bottom graphs show the mass fraction over the same density range.

Without diffuse heating, the mass fraction of gas in disk SFOnly above our cloud definition limit of $n_{\rm H,c} > 100\,{\rm cm}^{-3}$ is 0.43, 0.4 and 0.16 for simulation times $t = 100, 200$ and 300 Myr respectively. For disk SF+PEheat, the same output times have cloud mass fractions of 0.36, 0.46, 0.33. The rise in dense gas from 100 to 200 Myr when diffuse heating is present is evidence for the disk still fragmenting over this period.

Little evolution in the shape of the PDFs is seen over the course of the simulations once the initial conditions have produced a fragmented disk. In contrast to disk NoSF in TT09, we do not see a rise in high density gas over time, since stars now form in gas above $n_{\rm H,c} > 100\,{\rm cm}^{-3}$ and deplete the gas reservoir above this threshold. This will have an impact on the maximum cloud mass as will be seen in section 5.

In agreement with other simulations of galactic disks (e.g. Robertson & Kravtsov 2008; Tasker & Bryan 2008; Wada & Norman 2007), both our disks can be fitted with a log-normal tail to their volume-weighted PDFs. In disk NoSF in TT09, the fit to the 200 Myr and 300 Myr lines extended up to densities of $n_{\rm H} < 10^5\,{\rm cm}^{-3}$, but in these cases star formation removes gas to steepen the profile at the high density tip, making this fit not as good. This log normal fit from disk NoSF is shown in Figure 3 and has the form,

$$\mathrm{PDF} = \frac{1}{\sigma_{\rm PDF}\sqrt{2\pi}} e^{-\left(\ln x - \bar{\ln x}\right)^2/2\sigma_{\rm PDF}^2}, \qquad (7)$$

where $x = \rho/\bar{\rho}$ and $\sigma_{PDF} = 2.0$. It remains a good fit to both disks at $t = 200$ Myr, but by $t = 300$ Myr, star formation has significantly eroded the dense gas.

The one-dimensional Mach number, $\mathcal{M}$, for the star-forming high density tail of the PDF can be estimated from the azimuthally averages profiles in Figure 2. Before star formation significantly depletes the disk gas, the velocity dispersion, σ_g, is dominated by the in-place velocity motions, $\sigma_{\rm nt}$, which are of order $15\,{\rm kms}^{-1}$. In this high density region, the temperature of the gas is close to our cooling floor at 300 K (a fact that will also be seen in Figure 4), giving a $c_s = 1.8\,{\rm kms}^{-1}$. The Mach number is given by the ratio of these two values, $\mathcal{M} = \sigma_{\rm nt}/c_s \approx 8.3$.

From this and the value of σ_{PDF}, the nature of the turbulence production in the star-forming gas can be deduced. The two numbers are related via $\sigma_{\rm PDF}^2 = \ln\left[1 + b^2\mathcal{M}^2\right]$, where b is found to vary between $b \sim 1/3$ for solenoidal (divergence-free) turbulent modes and $b \sim 1$ for compressive (curl-free) modes (Federrath et al. 2008). For $\mathcal{M} = 8.3$ and $\sigma_{PDF} = 2.0$, we find $b = 0.88$, suggesting that compressive forcing is the dominant turbulent mode. This is consistent with the compressive nature of cloud collisions which are likely to be a driving force for the turbulence.

Removing gas from the high density tail of the PDF via star formation causes an increase in the fraction of gas at densities below $n_H < 1\,{\rm cm}^{-3}$. This effect is more pronounced in disk SFOnly, since the fraction of cloud gas has dropped by almost a factor of 3 between 100 and 300 Myr, compared with a maximum change of just 1.4 in disk SF+PEheat.

Despite its temporal continuity, the fraction of gas between $10^{-4} < n_H < 1\,{\rm cm}^{-3}$ in disk SF+PEheat is higher than for disk SFOnly, remaining close to the initial condition value. This gas is the warm ISM in which the clouds are embedded and, as seen in Figure 1, has a denser filamentary structure due to a smaller level of fragmentation.

The peak at low densities of $n_H < 10^{-4}\,{\rm cm}^{-3}$ corresponds to gas in the 1 kpc region above and below the disk plane. In the disk SFOnly, we see the density of this region increase over time as the high velocity dispersion seen in Figure 2 causes the disk scale height to increase. With diffuse heating, the disk settles to an initially thicker profile with a lower velocity dispersion in its less fragmented ISM, undergoing less evolution.

A two-dimensional representation of the evolution of the ISM is shown as density vs temperature contour plots in Figure 4. The upper two rows of plots show the gas volume distribution (top) and gas mass distribution (bottom) at times $t = 100, 200$ and 300 Myr for disk SFOnly while the lower six plots show the same distributions for disk SF+PEheat. Diagonal lines mark constant pressure with the values being representative of the Milky Way (Boulares & Cox 1990): The upper-most line is the estimated value for the total Milky Way pressure, $P_{\rm tot}/k_b = 2.8 \times 10^4$ K cm^{-3}. The lower two lines show the thermal pressure, $P_{\rm th}/k_b = 0.36 \times 10^4$ K cm^{-3}, and the thermal pressure excluding the hot gas component, $P_{\rm th,nohot}/k_b = 0.14 \times 10^4$ K cm^{-3}.

The distributions show that gas warmer than 10^4 K, the typical temperature for the warm interstellar medium (McKee & Ostriker 1977), lies largely in pressure equilibrium, although with a wide range of values that run over a continuous distribution of densities and temperatures. Without diffuse heating, gas in disk SFOnly that is cooler than this remains in pressure equilibrium until it approaches the floor in our radiative cooling curve at 300 K. This appears as a sharp spike in high mass and low volume density in all plots. The gas in this region is in the star forming clouds whose self-gravity causes them to be over pressurized with respect to the surrounding ISM. There is a perceptible decrease of gas in this spike over time as the cloud gas is converted into stars. Temperatures lower than the cooling curve minimum are achieved via adiabatic expansion.

With the addition of diffuse heating in disk SF+PEheat, cooler gas is warmed causing its pressure to increase. This results in a significantly thinner profile and gas below $T < 10^4$ K being out of pressure equilibrium. The smaller range of temperatures and densities in the warm ISM is indicative of the coherent structure of filaments we saw in Figure 1 and the lower velocity dispersion in Figure 2.

Overtime, both disk profiles broaden as cloud mergers

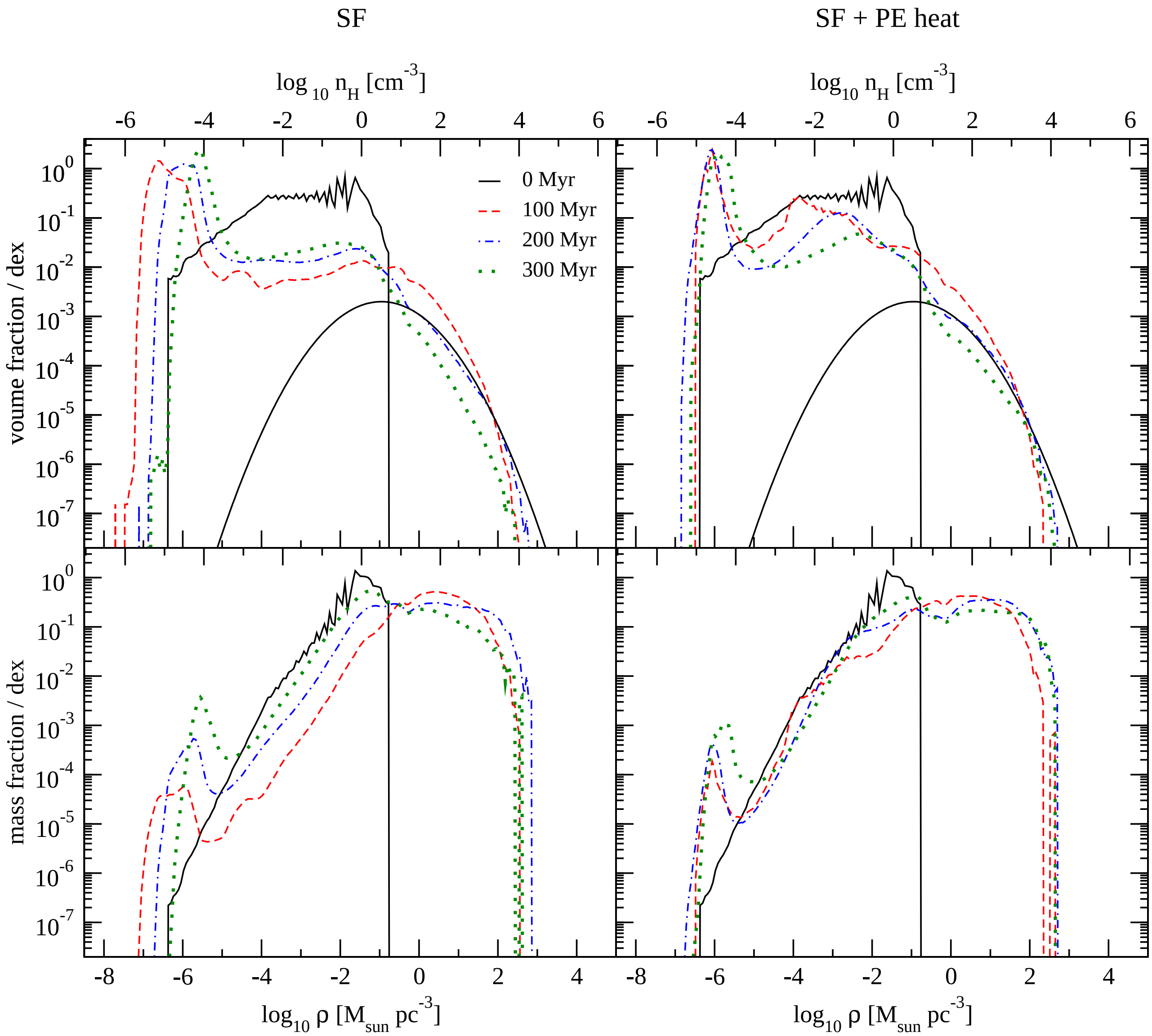

FIG. 3.— Probability distribution function (PDF) for the disks over the radii $2.5 < r < 8.5\,\mathrm{kpc}$ and height -1 kpc $< z < 1$ kpc. Left-hand plots are for the disk with only star formation (disk SFOnly) right-hand plots are for the disk where diffuse heating is included (disk SF+PEheat). The top panel shows the evolution of the volume-weighted PDF where the solid-line curve shows a log normal fit to the high density PDF tail. The bottom panel is the mass-weighted PDF. There is relatively little evolution in the PDF shape over the course of the simulation, although the depletion of gas in the SFOnly disk is evident in the gas fraction shift to lower densities. This is not as evident in SF+PEheat and more mass exists in the mid-density ($10^{-4} < n_H < 1\,\mathrm{cm}^{-3}$) ISM.

and tidal encounters disrupt the structure of the dense gas.

For the gas in pressure equilibrium at $T > 10^4\,\mathrm{K}$, its value is lower than that of the Milky Way in both the disks during the majority of the simulation. This is not surprising, since gas at this temperature will be strongly affected by sources of energetic feedback which we do not consider. We do see a rise in the pressure over time, resulting in a factor of 10 increase between $t = 100$ to $300\,\mathrm{Myr}$. Comparing with the results in disk NoSF, where no such increase was seen, we conclude this is the result of the localized potential created by the star particles.

5. THE PROPERTIES OF THE CLOUDS

While the galaxy's global structure concerns the entire ISM, its star formation occurs almost solely in the densest, coldest component of that gas. This cold phase is organized into the extended structures of the GMCs. As the disk cools and fragments, regions of gas exceed our threshold of $100\,\mathrm{cm}^{-3}$ and we recognize them as the GMCs. The properties of these entities dictate the environment in which stars will form and their birth, evolution and death will determine the star formation rate in the galaxy.

In this section, we focus on the properties of the identified GMCs, examining the the evolution of the clouds

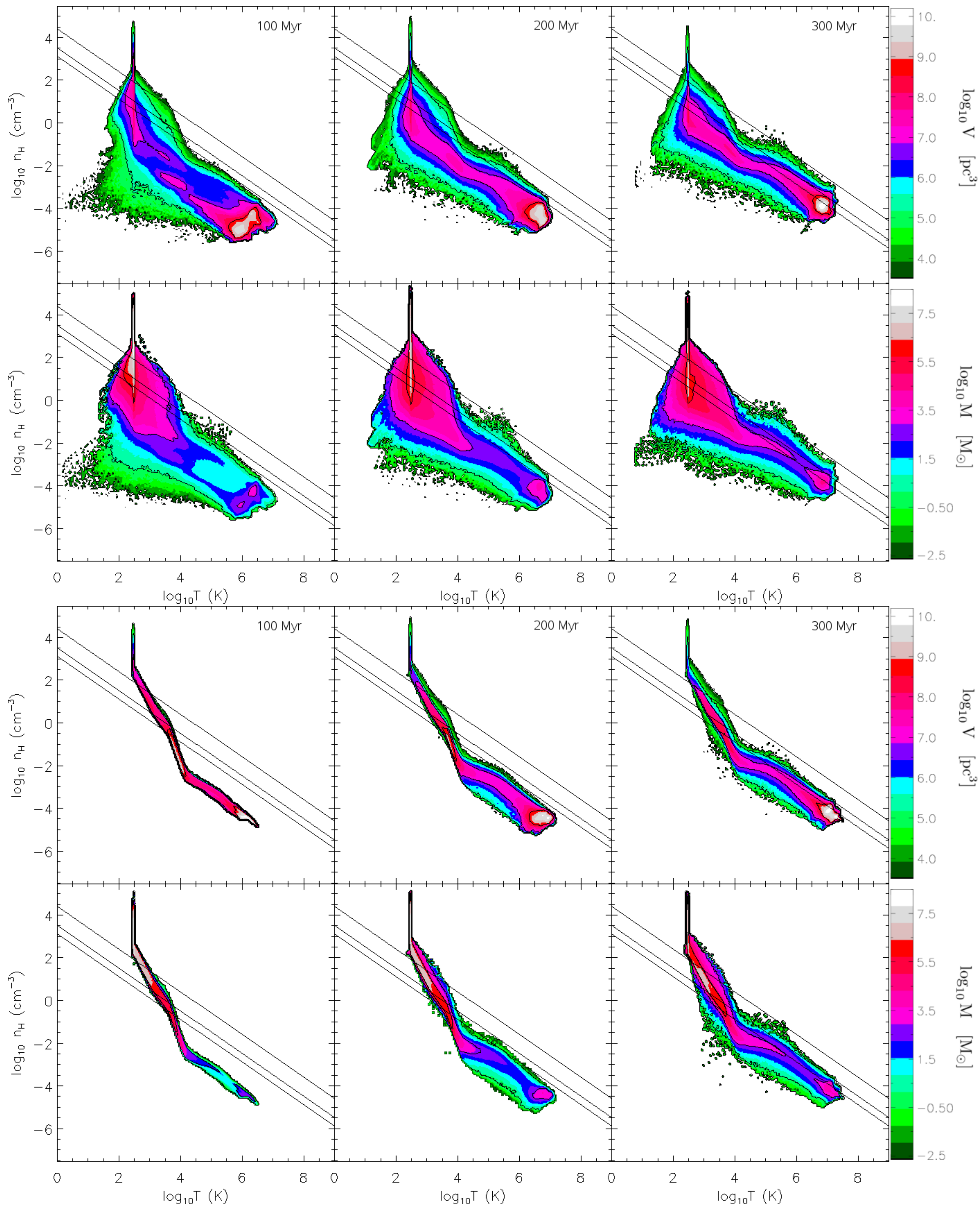

FIG. 4.— Density vs temperature contour plots for disk SFOnly (upper panel of six images) and disk SF+PEheat (lower panel of six). In each panel, the top row shows the distribution of gas volume while the bottom row shows gas mass for the region 2.5 kpc $< r <$ 8.5 kpc and -1 kpc $< z <$ 1 kpc. Solid lines show the total pressure in the Milky Way, $P_{\rm tot}/k_b = 2.8 \times 10^4$ K cm^{-3} (top), the thermal pressure, $P_{\rm th}/k_b = 0.36 \times 10^4$ K cm^{-3} (middle) and the thermal pressure excluding the hot gas component, $P_{\rm th,nohot}/k_b = 0.14 \times 10^4$ K cm^{-3} (bottom) (Boulares & Cox 1990). We see a continuous range of densities and pressures in both disks that is in pressure equilibrium above temperatures of 10^4 K and over-pressurized in the self-gravitating clouds. Diffuse heating greatly reduces the range of values due to the lower velocity dispersion and denser warm ISM.

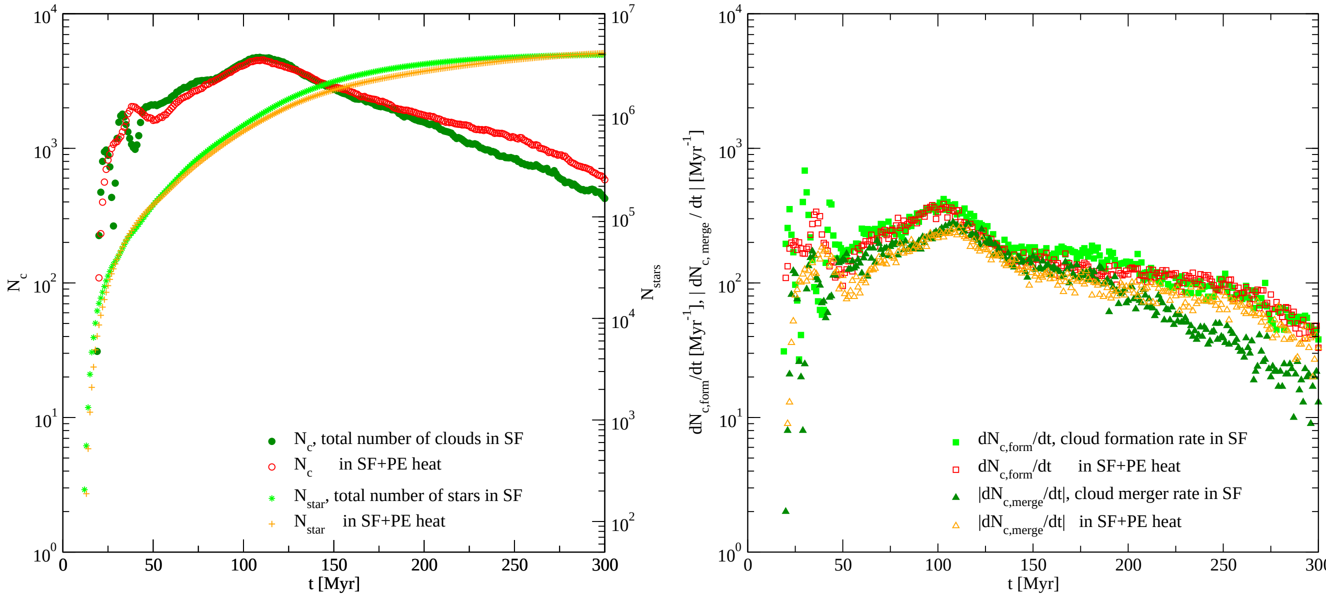

FIG. 5.— Left: Evolution of the total number of GMCs, N_c, (on left axis) and total number of star particles, $N_{\rm stars}$, (right axis) for both disks. Right: the GMC formation rate, $dN_{c,form}/dt$, and the GMC merger rate (equivalently, the rate of cloud destruction via mergers, since these are virtually all between two clouds), $|dN_{\rm c,merge}/dt|$ for both disks. The disk fragments over the first 100 Myr where the number of clouds begins to decrease due to mergers between clouds and gas depletion from star formation. The latter process is slower in the gas with diffuse heating, which suppresses the fragmentation of the disk and star formation in the clouds.)

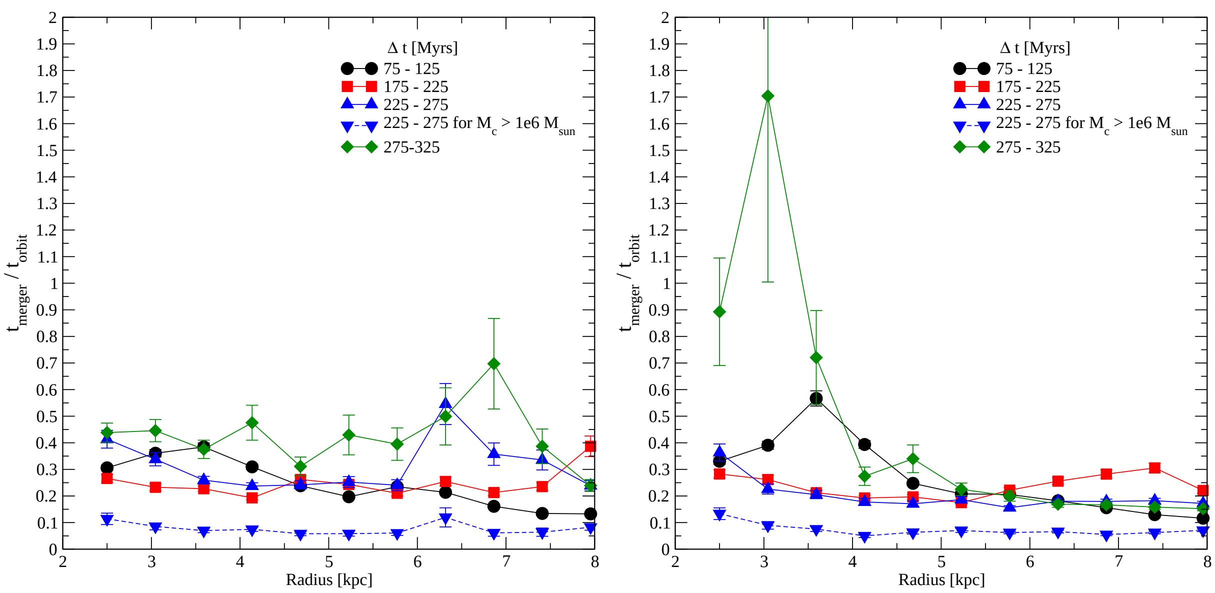

FIG. 6.— Cloud merger timescales, averaging over 50 Myr intervals of simulation time, for disks SFOnly (left) and SF+PEheat (right). Only clouds born after 140 Myr, the initial fragmentation of the disk, are included in the analysis. The average time for a merger is low at ~ 0.25 of an orbital period and largely independent of galactocentric radius. The dashed line shows the merger times of clouds with $M_c > 10^6\,{\rm M}_\odot$ (i.e., the average time for a cloud of that size to undergo a merger with a cloud of any mass), evaluated over the interval t = 225-275 Myr, which is lower by a factor of 2.

both as a function of simulation time, t, and as their age, or cloud time, t'.

The evolution of the cloud population itself is shown Figure 5 for both disks. The left-hand plot shows the total number of clouds and stars in the disk, while the right-hand plot shows the formation and merger rate of the clouds. The number of clouds initially increases as the disk gravitationally fragments, peaking at a rate of around $400\,\mathrm{Myr}^{-1}$ at 100 Myr in both disks. After that time, the disk is fully fragmented and both the cloud population and formation rate drop, accompanied by an increase in the number of star particles, as gas is consumed during star formation and mergers further erode the cloud population. There is a delay in the peak of the cloud formation rate and cloud merger rate that is equivalent to the mean merger rate between clouds. By 300 Myr, the cloud population has dropped by a factor of 10 without diffuse heating and a factor of 8 where diffuse heating was included. When diffuse heating is present, the build up of the stellar population is slightly more gradual, indicative of a slower star formation rate. By 300 Myr, the total number of star particles in both disks is approximately the same at ~ 4 million, but at 200 Myr, it differs by $\sim 20\%$. This accounts for the higher number of clouds in disk SF+PEheat at 300 Myr; the slower star formation rate allows the cloud time to accrete material as it is consumed, allowing a greater number to survive despite the ultimate star particle number being the same as in disk SFOnly.

Mergers between clouds happen throughout the course of the simulation, their rate related to the number of clouds in the disk. How mergers are recorded by the tracking algorithm is discussed in TT09, but in short, a merger is said to have happened when a single cloud is at the predicted position for two other clouds after 1 Myr of evolution, within a margin of twice the average radius of the potential merger product.

In the disk SFOnly, the number of mergers drops more steeply in the second half of the simulation compared to SF+PEheat. This corresponds to a steeper fall off in the number of clouds as the mass of gas above the cloud threshold density drops heavily as was seen in Figure 3. As we will see in Section 6, gas depletion in this simulation also causes the star formation rate to drop considerably over this period compared to the diffusely heated disk.

The frequency of the mergers in both disks are shown in Figure 6 as a function of the galactocentric radius. The merger time is computed as a fraction of the orbital time and averaged over 50 Myr. Merger rates over four time intervals during the simulation (75-125 Myr, 175-225 Myr, 225-275 Myr, 275-325 Myr) are plotted, where a merger is considered to be between two clouds. Cloud mergers involving more than two objects are negligibly rare.

There is no trend between merger rate and galactocentric radius for the majority of the simulation. At late times, disk SF+PEheat undergoes less mergers in its inner 4 kpc, corresponding to the drop in gas density (and so cloud number density) in that region, coupled with the lower velocity dispersion, as seen in Figure 2. In disk SFOnly, there is a spatially uniform increase at latest simulation time in the time between mergers, due to the reduced number of clouds seen in Figure 5.

Within the first three time frames, the average number of mergers is approximately constant in both simulations, with a value of ~ 0.25 of the orbital time, close to that seen in TT09 for disk NoSF. For our largest clouds, $M > 10^6\,\mathrm{M}_\odot$, this rate is lower by a factor of 2. This is in agreement with the calculations of Tan (2000), who estimated $t_{\mathrm{merger}}/t_{\mathrm{orbit}} = 0.2$ in an analytical model. Since the disk circular velocity is $v_c = 200\,\mathrm{kms}^{-1}$, the average time between interactions is ~ 30 Myr at a radii of 4 kpc. This is slightly higher than for the clouds in disk NoSF where an average time of 25 Myr was found, due to the star formation depleting the number of clouds.

The frequency of the cloud collisions is indicative that they play a major role in shaping the properties of the GMCs. What is less clear is what effect they have on the star formation rate as will be discussed in Section 6.

5.1. *GMC Properties with Simulation Time*

5.1.1. *Simulation Time: Cloud Property Distributions*

The properties of the individual clouds are shown in Figure 7 for disk SFOnly and Figure 8 for the clouds for disk SF+PEheat. The distributions are shown at three different times during the simulation; 100 (red dashed lines), 200 (blue dot-dashed lines) and 300 Myr (green dotted lines).

The top left plot, Figure 7 (a) and Figure 8 (a), show the profiles for the cloud gas mass. In difference to when no star formation occurred in disk NoSF and in agreement with the PDF plots in Figure 3, we do not see an increase in the cloud mass over the course of the simulation. Instead, star formation prevents the formation of a high mass tail and caps the maximum cloud mass at $M < 10^{6.7}\,\mathrm{M}_\odot$. When diffuse heating is included in Figure 8 (a), we see one outlier beyond this truncation at $M = 10^{7.1}\,\mathrm{M}_\odot$ which could be due to a recent merger event. Otherwise, the addition of heating does not change the mass cut-off.

The peak of the mass distribution appears at $10^{5.6}\,\mathrm{M}_\odot$ at 100 Myr after the start of the simulation in disk SFOnly and slightly lower, $10^{5.5}\,\mathrm{M}_\odot$, in disk SF+PEheat. This drop in peak mass is due to the heating term supporting the cloud against its own gravity, slowly the collapse to its maximum density. This was noted in the disk PDFs in Figure 3 and will be seen again below in the distribution of cloud surface densities.

Without diffuse heating, the conversion of gas into stars causes the peak to migrate to lower masses over time, moving to $10^{4.9}\,\mathrm{M}_\odot$ by 300 Myr. At this stage, 75 % of the clouds have a stellar mass fraction greater than 90 %. This high stellar content is due to the lack of feedback that would act to prevent gas continually collapsing to form stars within the cloud. With diffuse heating, the evolution of the mass profile is reduced, with no decrease in the peak position over time and a smaller evolution in the low mass end of the spectrum. This is in keeping with Figure 3 where we saw little change in the heated disk's ISM over time. Again, the added thermal support is the cause here, decreasing the cloud density and so increasing its dynamical time, causing a slower rate of conversion from gas into stars through equation 5.

Observations of the Milky Way by Williams & McKee (1997) find a truncation in the cloud molecular mass at $M_{\mathrm{u}} \sim 6 \times 10^6\,\mathrm{M}_\odot$. Since we follow all the neutral

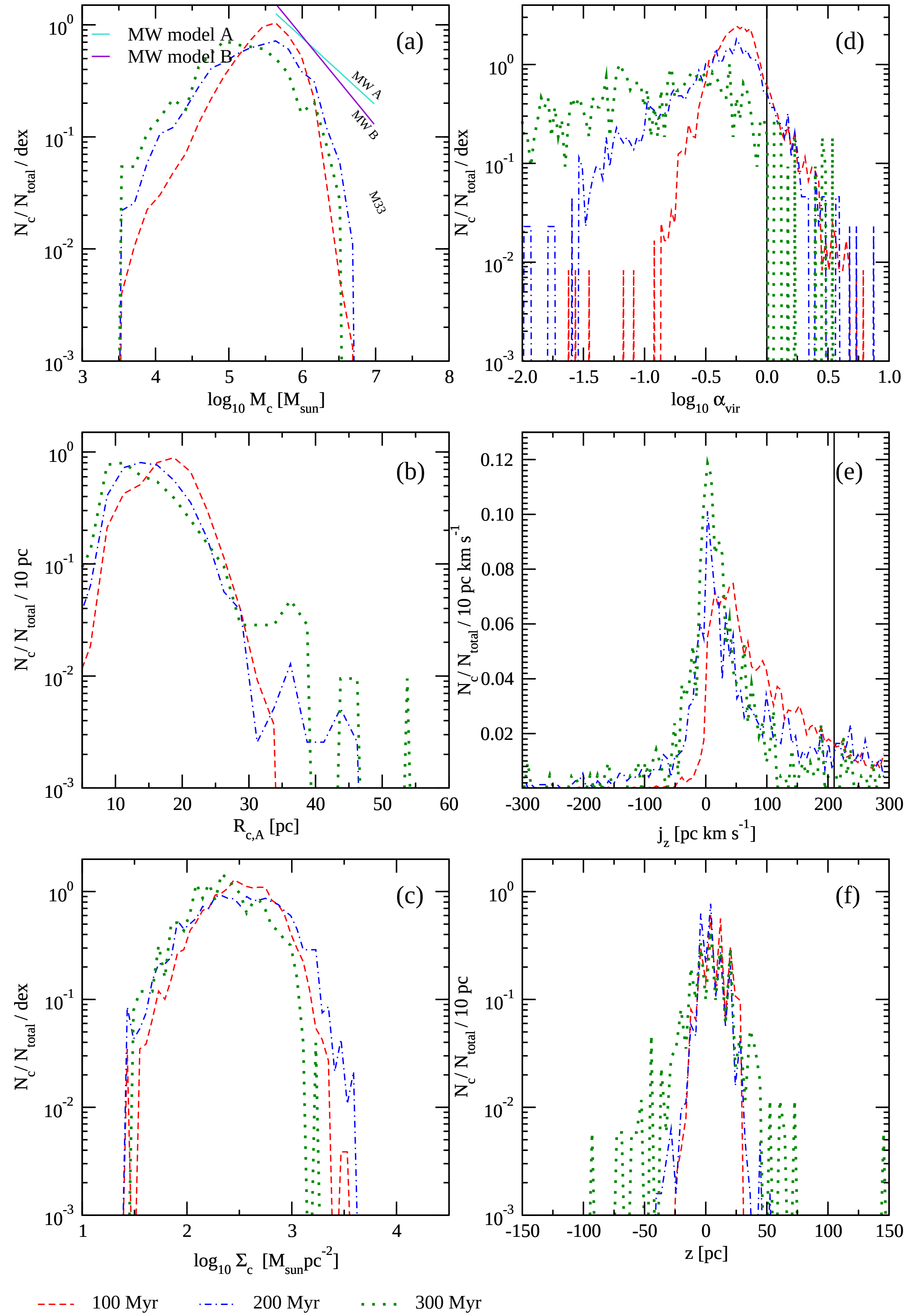

FIG. 7.— Normalized distributions of GMC properties at 100, 200 and 300 Myrs after the start of the simulation for disk SFOnly. Top left plot shows: (a) cloud mass distribution overlaid with fits to observational data from the Milky Way (blue and violet solid lines; Williams & McKee (1997)). Middle left, (b): the average radii of clouds, $R_{c,A} \equiv (A_c/\pi)^{1/2}$ where A_c is the projected area of the clouds in the Y-Z plane. Bottom left, (c): mass surface density of the clouds, $\Sigma_{c,A}$. Top right, (d): virial parameter, $\alpha_{\rm vir}$ with the vertical line indicating where $\alpha_{\rm vir} = 1$, the limit for gravitational binding. Middle right, (e): vertical component of the specific angular momentum vector, j_z. The vertical line indicates a value of j_z of a spherical ($\simeq 110$ pc radius) region of the initial conditions at galactocentric radius $r = 4$ kpc containing 10^6 M$_\odot$. Bottom right, (f): vertical height distribution, z, of the clouds.

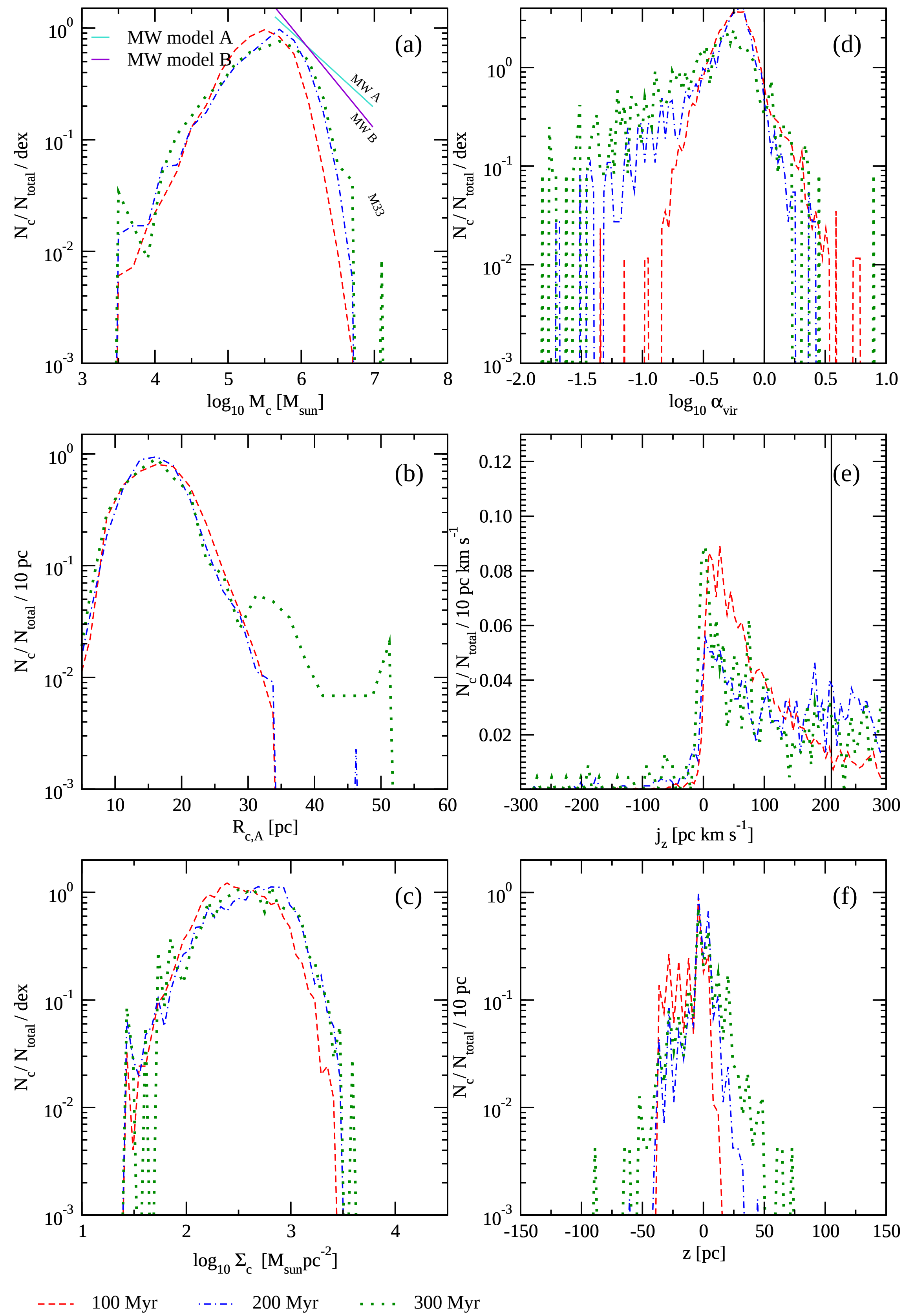

FIG. 8.— Normalized distributions of GMC properties at 100, 200 and 300 Myrs after the start of the simulation for disk SF+PEheat. Plots are the same as those described in Figure 7. Top left: (a) cloud mass, M_c. Middle left: (b) cloud radius, $R_{C,A}$. Bottom left: (c) mass surface density, Σ_c. Top right (d) virial parameter, $\alpha_{\rm vir}$. Middle right (e) vertical component of the specific angular momentum, j_z. Bottom right: (f) cloud center-of-mass vertical positions, z.

gas, our results also include an atomic envelope whose mass is estimated by Blitz et al. (1990) to be of order the molecular component. This would take the observed truncation limit up to $M < 1.2 \times 10^7\,\mathrm{M_\odot}$. Recent observations by Fukui et al. (2009) of the LMC, suggest smaller envelopes with 10% of the mass, providing a limit of $M_\mathrm{u} \sim 6.6 \times 10^6\,\mathrm{M_\odot}$. In both cases, our maximum mass falls below or close to the observed truncation.

This simulated mass spectrum can be compared to observations of GMCs in the Milky Way. These observations (and indeed, those in other galaxies such as M33 as found by Rosolowsky et al. 2003) fit a power law of the form $\frac{dN_c}{d\ln M_c} \propto M_c^{\alpha_c}$. The two lines on Figure 7 (a) and Figure 8 (a) show this relation for observations of α_c in the Milky Way made by Williams & McKee (1997). Their measured value for α_c depends on if the observed sample is assumed to be equally under-sampled at all masses ($\alpha_c = 0.6$, MWA) or if lower mass clouds are more under-sampled than high mass ($\alpha_c = 0.8$, MWB).

The distributions most appropriate to compare with these observations are the lines at 200 and 300 Myr, after the disk has settled and cloud interactions have become the dominant force in the ISM. Within the mass range $\sim (0.5 - 10) \times 10^6\,\mathrm{M_\odot}$, where our clouds are most resolved, we find that disk SFOnly approaches the Milky Way GMC population. With diffuse heating, the evolution of the mass profile is reduced, and the distribution is steeper at later times.

Williams & McKee (1997) estimate that, within the inner Milky Way, there are ~ 1000 clouds with $M_c > 10^5\,\mathrm{M_\odot}$ and 100-200 clouds with $M_c > 10^6\,\mathrm{M_\odot}$. At 200 Myr, we find for disk SFOnly 1122 clouds with $M_c > 10^5\,\mathrm{M_\odot}$ and 179 clouds with $M_c > 10^6\,\mathrm{M_\odot}$, in good agreement with this result. The cloud population in disk SF+PEheat is slightly larger with 1491 clouds with $M_c > 10^5\,\mathrm{M_\odot}$ and 238 with $M_c > 10^6\,\mathrm{M_\odot}$, reflecting the higher fraction of cloud gas at this time, but is still of the same order as the observations. Moreover, the mass fraction of clouds at 200 Myr is 0.4 for the disk without diffuse heating and 0.46 when it is included (as seen in section 4), coinciding with the estimated value of Wolfire et al. (2003) for the fraction of molecular to atomic gas inside the solar radius.

Figure 7 (b) and Figure 8 (b) show the average radius of the clouds defined as $R_{c,A} \equiv (A_c/\pi)^{1/2}$, where A_c is the projected area of the cloud in the $y-z$ plane (that is, as it would be measured by an observer embedded in the plane of the galaxy). Cloud radii are typically around 15 pc in both disks, in good agreement with observations of GMCs in the Milky Way and M33 (Lada et al. 2010; Rosolowsky et al. 2003). This is slightly smaller than the non-star forming clouds in disk NoSF (typical radius ~ 20 pc), but the inclusion of star formation has only significantly impacted the tail of the distribution which, as with the mass, is now prevented from continual growth.

As with the mass profile in Figure 7 (a), there is a decrease in the peak cloud radius over time for disk SFOnly, as gas is converted into stars. This is not reflected in disk SF+PEheat as its cloud mass fraction changes slowly under the influence of a lower SFR. At later times, there are a small number of extended structures which are likely to be from older clouds that have undergone multiple merger events.

Figure 7 (c) and Figure 8 (c) show the surface density of the clouds, $\Sigma_c \equiv M_c/A_c$. The distribution is the most robust property plotted, showing minimum evolution over time. The peak value sits $\sim 300\,\mathrm{M_\odot pc^{-2}}$, in agreement with disk NoSF, although at 100 Myr, disk SFOnly has a lower higher peak surface density than disk SF+PEheat, as the heating slows down the fragmentation to the highest densities.

There is a minor amount of evolution over time. Without diffuse heating, the surface densities drop as the clouds becomes more stellar dominated. With the diffuse heating, the shift is in the opposite direction as the disk self-gravity slowly overwhelms the support from heating and amount of cloud gas rises between 100 Myr and 200 Myr. Compared to the changes in mass and radius profile, however, these shifts are small.

The independence of the surface density profile to physics and time agrees with Larson (1981) and Solomon et al. (1987), who found that GMCs in the Milky Way had a constant surface density. Their measurements give a value for Σ_c lower than what we find, with $\Sigma_c = 200\,\mathrm{M_\odot pc^{-2}}$, but this does not take into account the atomic envelope, which can be a factor of 100 lower in density (Fukui et al. 2009).

The degree of gravitational binding in the clouds can be estimated by the alpha virial parameter, α_{rmvir}, plotted in Figure 7 (d) and Figure 8 (d). This quantity is defined as $\alpha_{vir} \equiv 5\sigma_c^2 R_{c,A}/(GM_t)$, where σ_c is the mass averaged velocity dispersion of the cloud, $\sigma_c \equiv (c_s^2 + \sigma_{nt,c}^2)^{1/2}$, with $\sigma_{nt,c}$ the one-dimensional rms velocity dispersion about the cloud's center-of-mass velocity (Bertoldi & McKee 1992). In contrast to TT09, M_t is now the sum of the total gas and stellar mass in the cloud. To calculate this, star particles are associated with the cloud if they reside within its boundaries or within a distance of twice its average radius. A value of $\alpha_\mathrm{vir} = 1.0$ states that a spherical, uniform cloud with negligible surface pressure and magnetic fields is virialized. This translates to a cloud for which $\alpha_\mathrm{vir} < 1.0$ being gravitationally bound and one for which $\alpha_\mathrm{vir} > 1.0$ likely to be unbound. Observationally, clouds are seem to be on the borderline of the two states, with $\alpha_{vir} \sim 1$ (McKee & Ostriker 2007).

For both our disks, the profile peaks at $\log(\alpha_{vir}) \sim -0.25$ throughout the simulation, implying our clouds are weakly bound. There is an increase in the fraction of more highly bound objects over time as the clouds become more stellar dominated, resulting in mergers increasing the cloud's total mass more than its gas fraction (which would increase its radius or surface density). This effect is strongest in disk SFOnly, with the distribution at 300 Myr showing an almost flat profile below $\alpha_\mathrm{vir} < 0.5$. As previously mentioned, 75% of the clouds at this time are now over 90% stellar in mass, the relatively small quantity of gas making it unlikely that our expression for α_{vir} can still apply. With diffuse heating this fraction is only $\sim 46\%$ and 300 Myr, and α_vir shows a smaller level of evolution.

The specific angular momentum in the vertical, z, component is shown in Figure 7 (e) and Figure 8 (e). The vertical line marks the specific angular momentum that a sphere of $10^6\,\mathrm{M_\odot}$ and radius $r = 4$ kpc has in the initial conditions. The clouds have an angular momentum much smaller than this, since they are much more com-

pact objects and therefore less susceptible to the disk sheer.

Without diffuse heating, the angular momentum profile in disk SFOnly is very similar to disk NoSF, with j_z decreasing over time, moving from an almost purely positive valued distribution to a broader profile where a substantial fraction of the clouds have a negative j_z. These clouds rotate in the opposite sense to the galaxy as will be discussed in section 5.1.3. This broadening is due to interactions between clouds affecting their rotation.

The diffuse heating once again moderates the evolution of the cloud distributions, causing j_z in disk SF+PEheat to show a smaller change over time. While cloud interactions are still common (as we saw in Figure 6), their effect on the cloud's rotation is moderated by the denser, filamentary structure of the surrounding ISM which maintains a low velocity dispersion as was seen in Figure2. This allows late forming clouds to form in a more structured, less turbulent environment than without diffuse heating, which plays a significant role in determining the rotation of the clouds.

The vertical distribution of the clouds is shown in the final panel, Figure 7 (f) and Figure 8 (f). The cloud scale height grows over the course of the simulation in both disks, due to the frequency of cloud collisions scattering clouds out of the galactic mid-plane. With the exception of our last time analysis which has a high degree of scatter, the scale height of the clouds is comparable to that of the GMCs in the Milky Way at $\lesssim 35\,\mathrm{pc}$ (Stark & Lee 2005). Diffuse heating makes little difference to this distribution, although we saw in Figure 3, that the scale-height of the warm ISM is initially larger in disk SF+PEheat due to the added pressure from the heating.

5.1.2. *Simulation Time: Velocity Dispersion vs Size Relation*

The internal cloud velocity dispersion plotted against cloud size is shown for clouds present at t=200 Myr in Figure 9 for both disks. Only clouds with mass greater than $M > 10^{5.5}\,\mathrm{M}_\odot$, whose internal structure has a reasonable chance of being resolved, are plotted. (This cut-off is slightly lower ($M > 10^{5.5}\,\mathrm{M}_\odot$) than in TT09 ($M > 10^{6}\,\mathrm{M}_\odot$) due to clouds being on average more massive). σ_c is the mass-averaged 1D internal velocity dispersion of the clouds viewed at a 52° inclination angle, similar to our view of M33.

Observed clouds in M33 (Rosolowsky et al. 2003) and the Milky Way (Larson 1981; Solomon et al. 1987) show a velocity dispersion (line width) that increases as a power of their radii. The fit for these two observed populations are also plotted in Figure 9. Unlike in disk NoSF, where we reproduced the observed relation over an order of magnitude, neither of our disks have a cloud population that shows a strong correlation between these two quantities. This is likely due to the restricted range of radii that the clouds now obtain, covering only a factor of four in range, compared to in disk NoSF where they extended over a factor of 10 without the inclusion of star formation to limit growth.

In part, this uniformity of our current cloud population radii is due to our initial conditions. We intentionally model clouds in an environment typical to the Milky Way at the solar radius. The range in disk surface density is only a factor of 10 as can be seen in Figure 2 and decreases over time. This means that any variation in cloud properties in our populations must come from their interactions and internal physics, not from variations in the galactic environment. The inclusion of energetic localized feedback might be expected to ease this issue and create a wider range of cloud radii.

The effect of diffuse heating in disk SF+PEheat slightly reduces the spread in σ_c, but otherwise has no impact. This is in difference to the effect on the warm ISM, where the presence of diffuse heating significantly reduced the velocity dispersion, as seen in Figure 2. The denser, self-gravitating cloud gas, however, is less altered by this term.

5.1.3. *Simulation Time: Distribution of the Angular Momentum Vector*

The distribution of angles, θ, between the cloud's own angular momentum vector and the galactic rotation axis is shown in Figure 10 for both disks at four simulation times; 50, 100, 200 and 300 Myr. θ for clouds in disk SFOnly are shown on the top panel while θ for the clouds in Disk SF+PEheat are in the lower panel. Clouds with $0 < \theta < 90$ rotate about their center of mass in the same sense as the galaxy's angular momentum vector and are considered to be *prograde* rotators. Clouds with $90 < \theta < 180$ rotate in the opposite sense to the galaxy and are *retrograde* rotators. As the first clouds begin to form in the disk, we see an almost purely prograde population for both simulations. These clouds predominantly feel only the disk sheer as cloud-cloud interactions are still low in the partially fragmented disk. As the simulation continues, a retrograde population of clouds develops and by 300 Myr, 30% of the clouds in the disk without diffuse heating rotate in the opposite sense to the galaxy. Clouds present at these later times feel not only the sheer of the disk, but also the gravitational pull from neighboring clouds, including the effect of mergers. While forming in this more complex environment, clouds can develop a retrograde motion, or be later scattered by neighboring clouds to switch their sense of rotation.

When diffuse heating is included in disk SF+PEheat, the fraction of clouds that develop a retrograde motion is significantly reduced, with only 12% rotating in a counter sense to the galaxy at 300 Myr. That this was true was indicated in Figure 8 (e), where the specific angular momentum profile contained only a small component with $j_z < 0.0$. As mentioned in section 5.1.1, this is the result of the denser warm ISM, whose filamentary structure acts to encourage the clouds to remain prograde.

The effect of the ISM environment on cloud properties was also noted by Dobbs (2008) in their single fluid model of the ISM. In their disk simulation using an isothermal warm gas, no clouds arose with retrograde rotation, a fact they attribute to the absence of a clumpy medium required to cause collisional interactions between clouds. In our model, the ISM is fully multiphase, but the diffuse heating has increased the density and structure of the warm gas. We do not find a decrease in the number of cloud mergers, but similarly to Dobbs (2008), we find the warm ISM is playing a significant role in determining the cloud rotation.

The result that the disk environment can impact the cloud properties is particular interesting, since that was

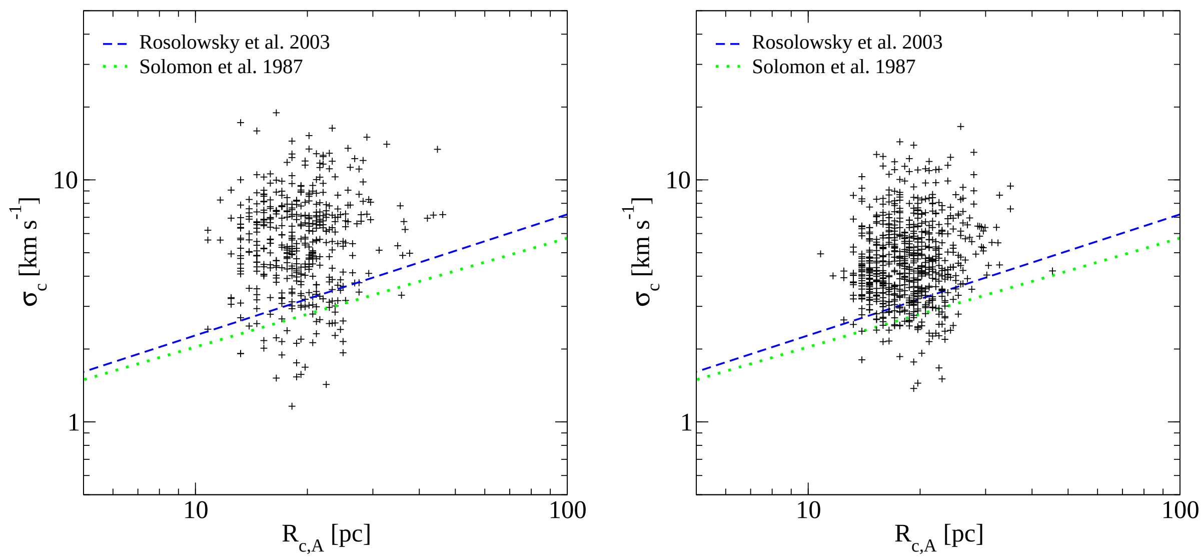

FIG. 9.— Cloud velocity dispersion vs size relation for clouds with mass $M > 10^{5.5}\,\mathrm{M_\odot}$ at t = 200 Myr. Clouds in disk SFOnly are plotted in the left-hand pane and clouds in disk SF+PEheat are plotted on the right. σ_c is the line of sight velocity of the clouds in the galaxy viewed at 52° inclination angle, similar to our view of M33. The dashed blue line shows the result (slope and normalization) of the Rosolowsky et al. (2003) study of massive ($10^5\,\mathrm{M_\odot} \lesssim M_c \lesssim 10^6\,\mathrm{M_\odot}$) GMCs in M33, with an exponent of 0.45 ± 0.02. The green dotted line shows the result of the Solomon et al. (1987) study of Galactic GMCs with an exponent of 0.5 ± 0.05. No obvious trend is seen in our results due to the limited range of radii of the clouds.

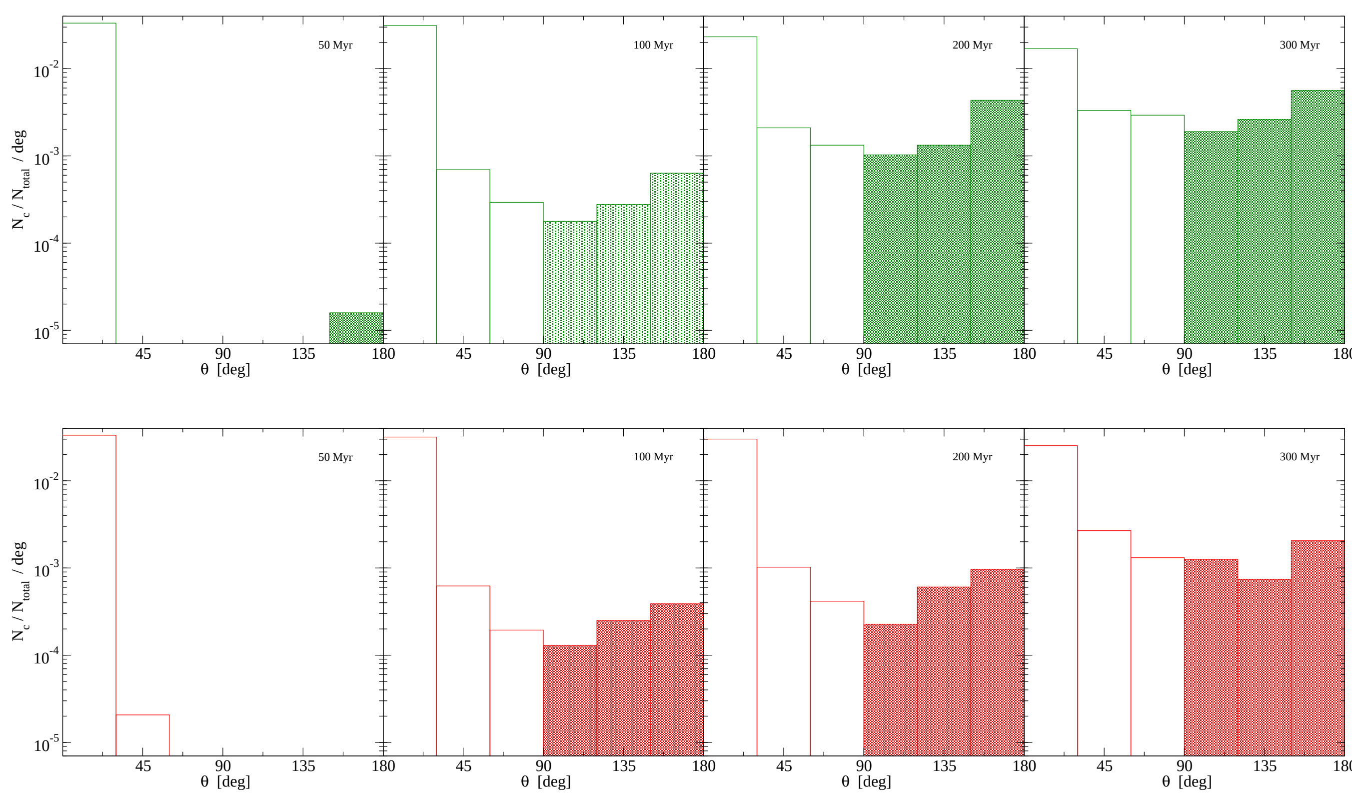

FIG. 10.— Distribution of the angle between the cloud angular momentum vector and the galactic rotation axis at different times over the course of the simulation. The distribution for clouds in disk SFOnly is shown in the top panel and in disk PEheat in the bottom panel. The shaded bars indicate retrograde motion. The presence of diffuse heating significantly decreases the number of retrograde clouds at late times. By 300 Myr, the number of retrograde clouds has reached 30% in the disk without diffuse heating and 12% in the disk with heating.

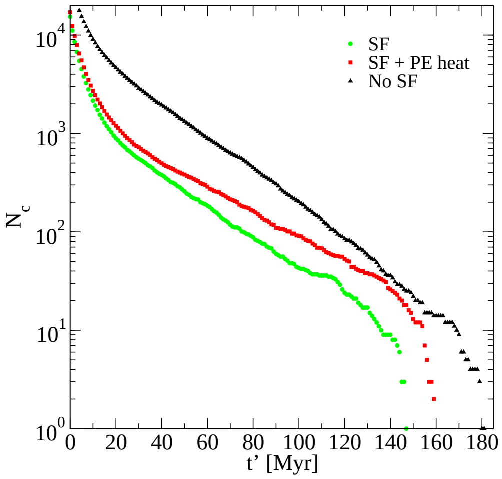

Fig. 11.— Distribution of cloud lifetimes in the simulations. Green circles show the clouds in disk SFOnly. Red squares depict clouds in disk SF+PEheat and black triangles show the results from disk NoSF. The majority of clouds live only a few Myr with only of order 0.5% reaching 100 Myr. This high end tail is probably due to the lack of energetic feedback.

not a previous prediction from analytical models or observations. In disk NoSF, the percentage of clouds that develop a retrograde motion was equal to disk SFOnly, supporting the claim that it is the difference in the warm ISM that controls the development of retrograde motion.

Observations by Rosolowsky et al. (2003) find a 40% split between prograde and retrograde clouds in the sample of GMCs in M33. Both our disks support the hypothesis that interactions between self-gravitating clouds are responsible for the distribution in angular rotation.

5.2. *GMC Properties with Cloud Age*

By tracking the clouds through the simulation over time, as described in section 2.2, we are able to compare properties of clouds that have the same age, t', but exist at different simulation times. To avoid our results being affected by the initial fragmentation of the disk (during which cloud interactions are low) we only consider clouds born after 140 Myr in our analysis.

The spread of ages in the clouds of our simulations are shown in Figure 11. In the two simulations presented in this paper, the vast majority of clouds only live between $t'_{\rm age} = 0 - 20$ Myr. This number drops by half after 3 Myr and by a factor of ten by 20 Myr. Of the 7% that live longer than this, only 0.5% survive to 100 Myr.

Without star formation, the decrease in cloud number is steady with age, as cloud destruction occurs purely as a function of the merger rate which is approximately constant. The addition of star formation increases the cloud mortality rate by a factor of 3-4 by a cloud age of 10 Myr, having the greatest impact on the younger, less massive clouds (see below for details of the evolution in the cloud mass). It is likely these very young objects are forming close to other clouds who they almost immediately merge with, or that their smaller size causes them to be disrupted quickly by star formation.

Including the diffuse heating in disk SF+PEheat decreases the star formation rate and allows clouds to live longer. It has the most effect on older clouds, whose higher mass makes them more resilient to mergers and hence their death is controlled primarily by their star formation.

The lifetimes of GMCs is still a matter of intense debate. A current prevailing point of view, however, is that GMCs live 1-2 dynamical times, putting their age in the range of 5-20 Myr (McKee & Ostriker 2007; Murray 2010). This agrees well with our clouds, a surprising result since we include no form of energetic feedback which has been considered to be one of the main factors in cloud destruction.

5.2.1. *Cloud Time: Cloud Property Distributions*

The properties of the clouds as a function of their age are shown in Figures 12 (disk SFOnly) and 13 (disk SF+PEheat) for the same distributions plotted in Figure 7 and 8; cloud mass, radii, surface density, virial parameter, vertical component of the angular momentum and their vertical distribution. The solid black line shows recently formed clouds that are less than 1 Myr old. The red dashed line shows the distributions for clouds between 9-10 Myr old, the estimated observed age for a GMC. The blue dot-dashed line is for cloud ages 49-50 Myr and the green dotted line for clouds 99-100 Myr old. These two last lines show the properties of the older clouds in the simulation although, as shown in Figure 11, significantly fewer clouds live to these ages, with only 44 clouds forming the distribution of the 99-100 Myr profiles in disk SFOnly and 92 clouds in disk SF+PEheat.

In both the disks, we see that older clouds are on average more massive, have larger radii, higher surface density and are slightly more gravitationally bound. These trends are more pronounced than in disk NoSF since the gas depletion from star formation destroys a large number of younger clouds, as seen in Figure 11. Clouds with masses $M \lesssim 10^5\,_{\odot}$ are particularly prone to early mortality through star formation and mergers. The clouds that survive their early years are more massive, accumulating gas through accretion and mergers at a faster rate than their star formation can deplete it. This effect is most marked in disk SFOnly. In disk SF+PEheat when diffuse heating is present, less clouds with masses $\lesssim 10^5\,{\rm M}_{\odot}$ are born due to the additional heating increasing the Jeans length, raising the size of an object formed through gravitational collapse. This reduces the evolution of the low mass distribution at in the first 10 Myr of the cloud's life.

In contrast to this, the distributions of vertical angular momentum, Figure 12 (e) and Figure 13 (e), and vertical position above the disk, Figure 12 (f) and Figure 13 (f), are largely independent of cloud age. Without diffuse heating, newly formed clouds in disk SFOnly have a very low vertical angular momentum, causing the distribution to be sharply peaked. Cloud interactions later broaden this profile slightly and reduce the peak, but the form remains largely unchanged. When diffuse heating is present in disk SF+PEheat, the clouds are born with a wider range of positive (prograde) angular momentum values that also show little change over time. The filamentary structure of the ISM has produced a more dominantly prograde cloud population as seen in Figure 10, and the higher values of j_z means the probability of later producing a retrograde cloud in a cloud collision is low.

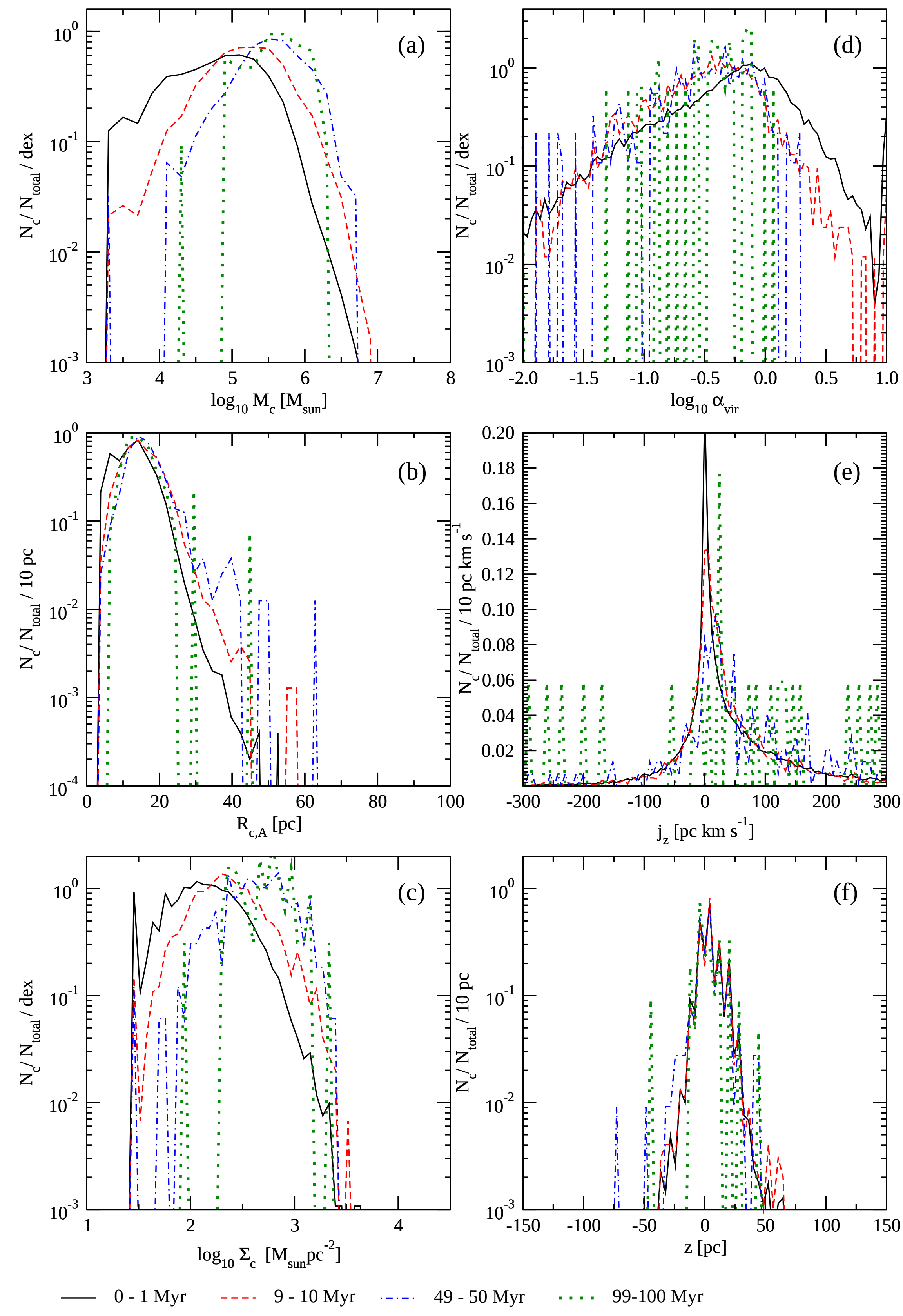

FIG. 12.— Normalized distributions of the GMC properties described in Figure 7 for disk SFOnly, but now showing results for different cloud ages: 0-1 Myr (solid lines), 9-10 Myr (dashed lines), 49-50 Myr (dot-dashed lines) and 99-100 Myr (dotted lines). All clouds in this analysis were born after 140 Myr of disk evolution, i.e. in the fully fragmented phase. Top left, (a): cloud mass, M_c. Middle left, (b): cloud radius, $R_{C,A}$. Bottom left, (c): mass surface density, Σ_c. Top right, (d): virial parameter, $\alpha_{\rm vir}$. Middle right, (e): vertical component of the specific angular momentum, j_z. Bottom right, (f): cloud center-of-mass vertical positions, z.

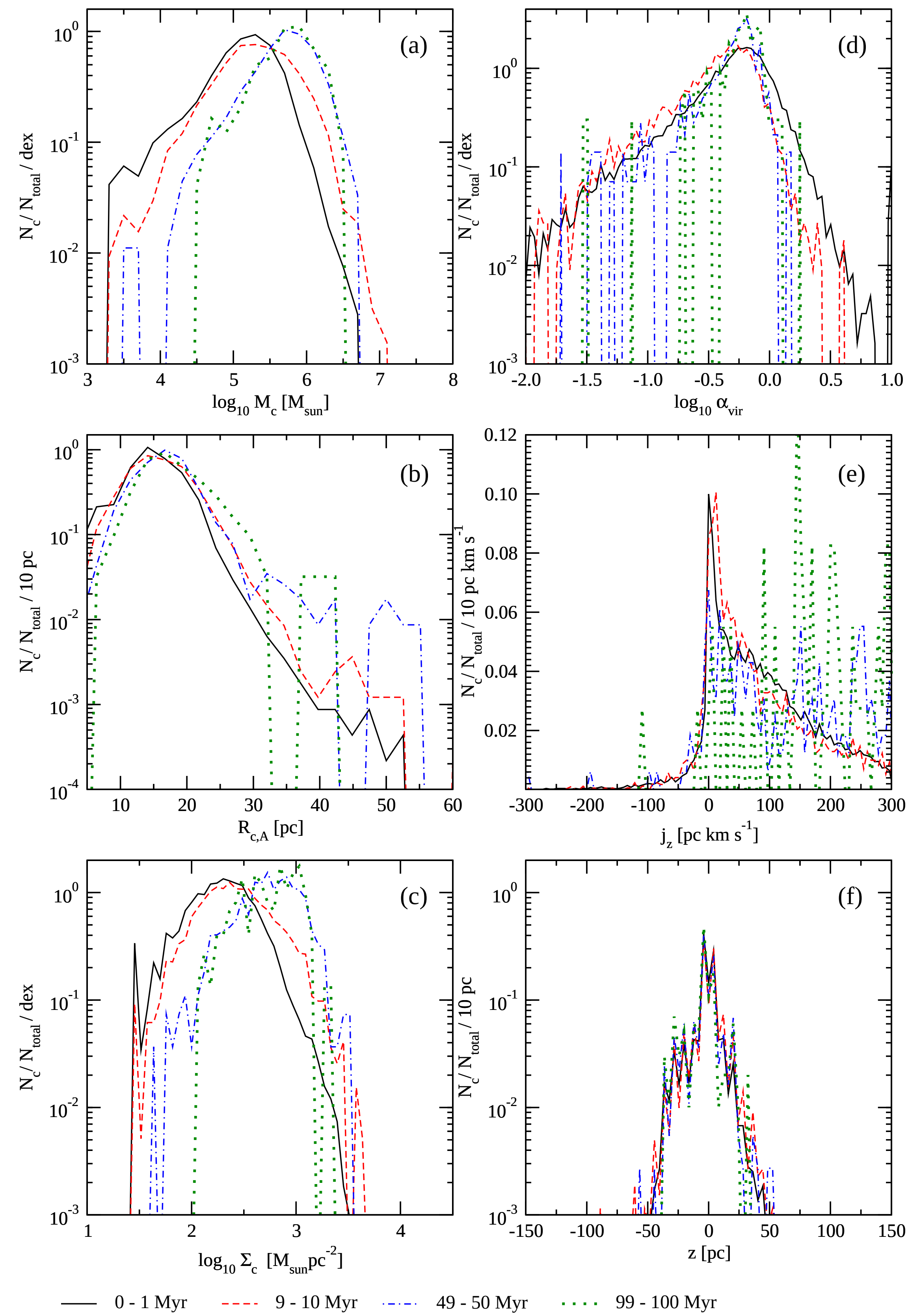

FIG. 13.— Normalized distributions of the GMC properties, as described in Figure 8 for Disk SF+PEheat, for cloud ages: 0-1 Myr (solid lines), 9-10 Myr (dashed lines), 49-50 Myr (dot-dashed lines) and 99-100 Myr (dotted lines) for clouds born after 140 Myr of disk evolution, i.e. in the fully fragmented phase. Top left, (a): cloud mass, M_c. Middle left, (b): cloud radius, $R_{C,A} \equiv (A_c/\pi)^{1/2}$. Bottom left, (c): mass surface density, Σ_c. Top right, (d): virial parameter, $\alpha_{\rm vir}$. Middle right, (e): vertical component of the specific angular momentum, j_z. Bottom right, (f): cloud center-of-mass vertical positions, z.

5.2.2. *Cloud Time: Distribution of the Angular Momentum Vector*

The robustness of the angular momentum with respect to cloud age is shown in the distribution of angles, θ, between the cloud angular momentum vector and the galactic rotation axis plotted in Figure 14. Clouds at four different ages are shown; newly born clouds with $t' < 1\,\mathrm{Myr}$, then clouds with ages $t' = 9-10\,\mathrm{Myr}$ and $49-50\,\mathrm{Myr}$ and finally our oldest clouds with $t' = 99-100\,\mathrm{Myr}$. The top panel shows the distribution of θ for disk SFOnly while the lower panel shows the distribution for clouds in disk SF+PEheat. As with Figure 10, the shaded bars show angles that equate to a retrograde rotation.

The percentage of retrograde rotating clouds remains about 25% for all age ranges in disk SFOnly and about 10% in disk SF+PEheat. Since all these clouds are born after 140 Myr in the simulation, they feel the forces from the fully fragmented disk, in addition to the sheer. The gravitational interactions from neighboring clouds on the newly forming bodies cause the retrograde population to form. As we can see from the first panel of Figure 10, clouds forming in pristine gas are always prograde.

As we have seen previously, the effect of diffuse heating is to reduce the fraction of retrograde clouds, due to the filamentary structure of the warm ISM having a strong impact on the newly forming clouds.

6. STAR FORMATION

The star formation history for the disk is plotted in Figure 15. As with the cloud formation history in Figure 5, the star formation initially increases steeply as the disk fragments. It reaches a peak value around 125 Myr and then declines steadily as gas is consumed in the disk.

At 200 Myr, the star formation rate is $15\,\mathrm{M_\odot yr^{-1}}$ for disk SFOnly and $17\,\mathrm{M_\odot yr^{-1}}$ for disk SF+PEheat. By the end of the simulation, this has dropped to $3\,\mathrm{M_\odot yr^{-1}}$ and $10\,\mathrm{M_\odot yr^{-1}}$, respectively, although the lower numbers are purely a factor of the gas depletion. The Milky Way is estimated to have a star formation rate of order $1-3\,\mathrm{M_\odot yr^{-1}}$ (Murray & Rahman 2010; Williams & McKee 1997). The fact we are higher than this though, is not surprising due to our lack of localized feedback.

The addition of diffuse heating in disk SF+PEheat initially reduces the fraction of dense cloud gas in the disk, as we saw in Section 4, causing the SFR to be lower over the first $\sim 175\,\mathrm{Myr}$ than when heating was not included. This causes the gas to be depleted in the disk at a slower rate, resulting in more gas being available at later times. This can be seen in Figure 16 which shows the distribution of the fraction of mass in stars for the clouds present at three different simulation times. Early in the simulation, clouds are gas dominated with a low (< 0.1) stellar fraction. By 300 Myr, a large fraction of the gas has converted into stars, making the majority of the clouds strongly stellar dominated. This is especially true for clouds in disk SFOnly, where 3/4 of the clouds have a stellar fraction > 0.9 by the end of the simulation. This inevitably causes the star formation to decrease and after 175 Myr, the star formation rate in disk SFOnly has dropped below the rate in disk SF+PEheat because the gas abundance has become too low.

The Kennicutt-Schmidt relation is an empirical measurement of the relationship between the surface SFR, Σ_{sfr}, and the surface gas density, Σ_{gas}, in a galaxy. It describes how efficiently a galaxy is converting gas into stars and takes the form shown in Equation 3. The value of the exponent, α_{sfr}, has been measured by several groups (e.g. Kennicutt 1998; Wong & Blitz 2002; Bigiel et al. 2008) for both the Milky Way and other galaxies and found it to vary between $\alpha_{\mathrm{sfr}} \approx 1-3$. Most recent work (Bigiel et al. 2008; Wong & Blitz 2002) suggests that the correlation is truly with molecular gas, $\Sigma_{\mathrm{H_2}}$, rather than total gas, $\Sigma_{\mathrm{gas}} = \Sigma_{\mathrm{HI}} + \Sigma_{\mathrm{H_2}}$, for which $\alpha_{\mathrm{sfr,H_2}} = 1.0 \pm 0.2$. When averaged with the atomic component, the exponent increases before the relation breaks down around $\Sigma_{\mathrm{gas}} \approx 10\,\mathrm{M_\odot pc^{-2}}$ in the outer regions of the disk where the gas becomes saturated with HI.

Figure 17 shows this relation plotted for our disks at $t = 200\,\mathrm{Myr}$. The diagonal lines mark constant star formation efficiency and the black crosses show the observations from The HI Nearby Galaxy Survey (THINGS) (Bigiel et al. 2008). For these observations, the fall-off around $10\,\mathrm{M_\odot pc^{-2}}$ is due to the dominance of atomic gas, with the points at higher densities with $\alpha_{\mathrm{sfr}} = 1.0 \pm 0.2$ being purely from molecular H_2. The results for disk SFOnly are shown by green filled symbols while disk SF+PEheat is marked in red open symbols. Square symbols show the result of averaging over an area of 750 pc across around each cloud, the equivalent spatial resolution to the THINGS survey. The circles show the quantities averaged over the individual clouds themselves, with area of order 15 pc across.

For equivalent spatial resolution (squares) we see that our star formation rate is higher than the observations by a factor of 10 in both our simulations. This agrees with what we saw in Figure 15 and is likely due to not having a source of localized feedback. The gradient here is $\alpha_{\mathrm{sfr}} 1.77$ for the disk without diffuse heating and 1.81 for when heating is included. This is steeper than the fit for the molecular gas found by Bigiel et al. (2008), but in closer agreement with the gradient of the atomic gas. Given the size of the region we are averaging over, compared to our cloud size, we would expect our result to be atomic gas dominated.

When averaged over individual clouds, the gas surface density is higher by approximately a factor of 100, compared with averaging over a larger area. In this volume, we can assume that the gas is at least 50% molecular, depending on the mass of the assumed atomic envelope. The fitted gradient for both these cloud populations is 1.27, slightly steeper than the result from (Bigiel et al. 2008), likely due to this mix of atomic and molecular gas.

Note, that neither sets of points gets a gradient of 1.5, as would be expected if our results were simply a product of having a constant star formation efficiency term, as given in Equation 5.

Despite having a lower SFR over the first 2/3 rds of the simulation, we do not see any great differences between the cloud populations with and without diffuse heating. From Figure 15, we can see that at our time of analysis, t = 200 Myr, the SFRs in both simulations are approximately constant. However, the same plot at t = 150 Myr shows no greater disparity between them, due their difference in SFRs being accompanied by similar differences in gas surface density, as was seen in Section 5.1. There

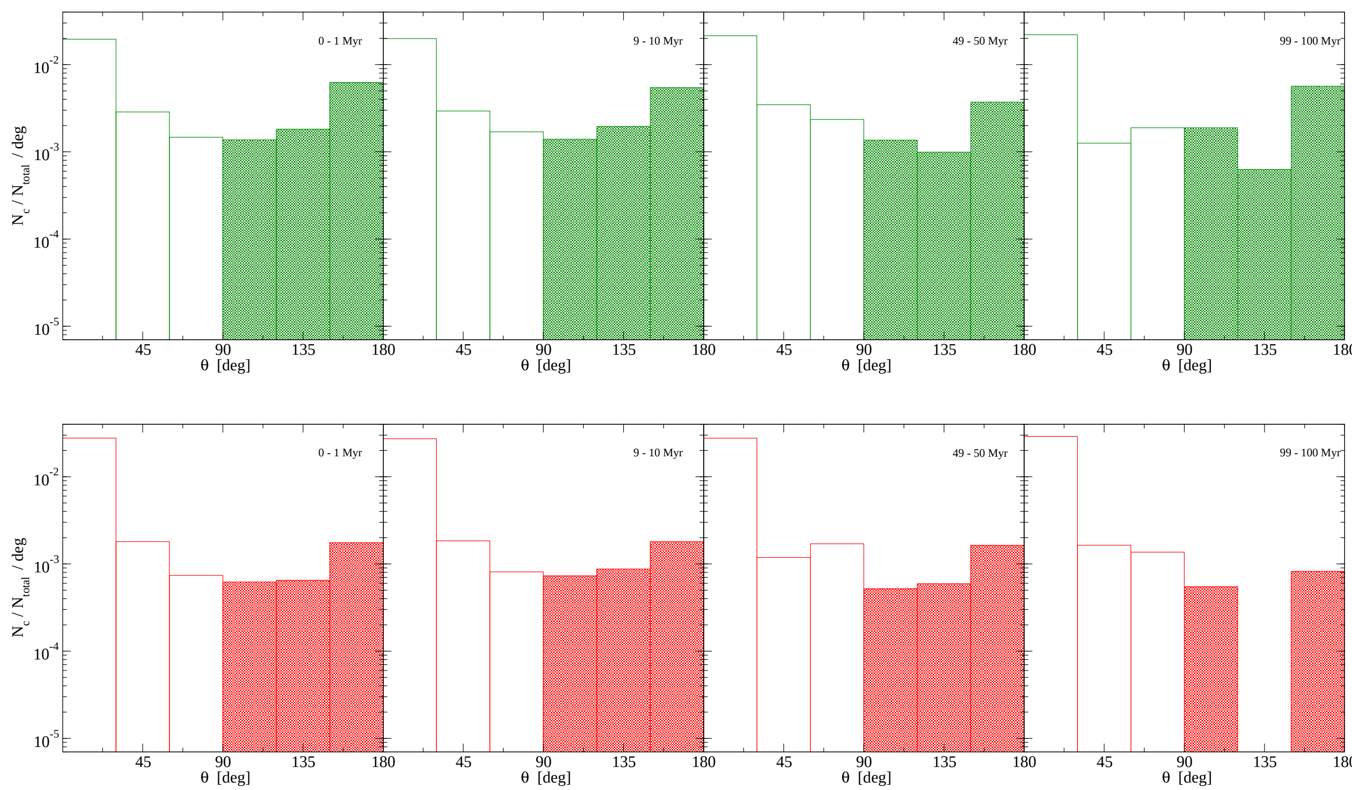

FIG. 14.— Distribution of the angle between the cloud angular momentum vector and the galactic rotation axis for clouds of different ages, born after 140 Myr, in disk SFOnly (top) and disk SF+PEheat (bottom). The shaded bars indicate retrograde motion. The percentage of clouds rotating retrograde in the top row is 28%, 26%, 18%, 25% respectively for each panel and 9%, 10%, 8%, 4% for the bottom row.

is slightly less scatter in the simulation that includes the heating term, especially when averaged over $750^2\,\mathrm{pc}^2$, due to the less fragmented ISM distribution.

Focusing on the individual clouds, the specific star formation rate (SSFR; the star formation rate per unit mass) can be plotted as a function of the cloud's gas mass. In their recent paper, Lada et al. (2010) measure the SFR in eleven GMCs in the Milky Way. They find a linear dependence with the cloud's mass, specifically SSFR$=\ 4.6 \pm 2.6 \times 10^{-8}\,\mathrm{yr}^{-1}$. The relation for our clouds is plotted in Figure 18 for the SSFR averaged over one dynamical time. The left-hand plot shows the results for disk SFOnly and the right-hand plot for disk SF+PEheat. Black circles show binned data for the complete cloud sample while the red squares and blue triangles only include clouds that have undergone a merger in the last dynamical time, with the latter considering only major mergers with a cloud mass ratio less than 2.0.

The upper dotted line shows the value from Lada et al. (2010). With the exception of the most massive clouds, our star formation rate is lower by a factor of 3-4. However, Lada et al. (2010) calculate the cloud mass from gas above a threshold surface density of $\Sigma_{\rm gas} \approx 116\,\mathrm{M}_\odot\mathrm{pc}^{-2}$, which they estimate is equivalent to a volume density of $n_{\rm H_2} \approx 10^4\,\mathrm{cm}^{-3}$. While our clouds larger than $M \approx 10^5\,\mathrm{M}_\odot$ achieve this surface density, their volume density is much lower, with the majority of clouds having average densities between $10^2 - 10^3\,\mathrm{cm}^{-3}$. If we reduce the Lada et al. (2010) SSFR value by a factor of 10 to allow for this, we get the lower dotted line. Our cloud SSFR largely lie above this lower line, suggesting that the SFR per cloud is too high, given the resolution, by a factor of 10 in agreement with Figure 17 for the disk averages over the same spatial scale as the observations.

For clouds with masses $M < 10^{5.5}\,\mathrm{M}_\odot$, the SSFR is approximately constant. At first sight, this seems to be in agreement with the Lada et al. (2010) result, however this population of clouds are at our resolution limit where their internal structure cannot be resolved well. In our cloud population, density scales with mass so larger objects have shorter dynamical times, increasing their SSFR. In this region where our results are not resolution limited, $M \gtrsim 10^5\,\mathrm{M}_\odot$, we therefore find that the SSFR is proportional to the cloud mass.

This result remains when we introduce diffuse heating in the right-hand plot of Figure 18. The maximum SSFR however is less, in agreement with our previous findings, and there is evidence of a down turn at high masses. This small population of very massive ($> 10^{6.5}\,\mathrm{M}_\odot$) clouds are extended structures from recent mergers, resulting in them having a lower density.

As we saw in Figure 6, mergers between clouds are a common occurrence and likely to have a significant impact on the clouds evolution. Tan (2000) suggested that such collisions could trigger star formation, providing a way of connecting local-scale motions with the globally observed Kennicutt-Schmidt relation. In Figure 18, however, we find that the presence of a recent merger decreases the clouds SSFR. This effect is even greater if the

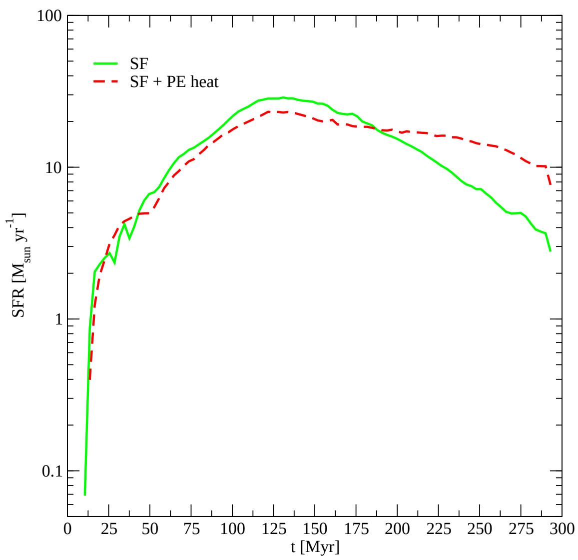

FIG. 15.— The star formation rate over the course of the simulation for disk SFOnly (green solid line) and SF+PEheat (red dashed line). Like the cloud population, the SFR peaks shortly after the disk has become fully fragmented. As gas is converted into stars and depleted from the clouds, it begins to drop. This decrease in SFR is significantly slower when diffuse heating is included, dropping to a value of $10\,\mathrm{M}_\odot\,\mathrm{yr}^{-1}$ rather than $3\,\mathrm{M}_\odot\,\mathrm{yr}^{-1}$ when diffuse heating is not included. Around 200 Myr, before gas depletion has removed most of the gas in the clouds with no diffuse heating, the SFR is greater than the estimated Milky Way value by a factor of 10. This is probably due to the lack of localized feedback.

merger was a major one with a cloud whose mass was at least 50% of the object it merged with. The impact of the mergers depends on mass, with larger clouds being unaffected unless experiencing a major merger. This is not hard to understand, since a more massive cloud will be undergoing predominantly collisions with much smaller objects which will cause less perturbations to its internal structure. The reason for the drop in SSFR is due to a corresponding drop in the cloud density. However, such a result is liable to be resolution dependent, due to the difficulties in resolving the changes to the clouds' internal structure across only a few cells. Federrath et al. (2010) finds that 30 cells are required to resolve a vortex within a cloud, while local box simulations with resolutions on the sub-parsec scale suggest that low density ($n_H = 3\,\mathrm{cm}^{-3}$) colliding flows can trigger local star formation by initiating gravitational collapse (Heitsch et al. 2008). If this applies to higher density collisions, then it is probable that cloud collisions could help, rather than hinder, star formation.

7. CONCLUSIONS

We investigated the formation and evolution of the GMC population formed in two isolated, Milky Way-type galaxies at a resolution $\lesssim 10\,\mathrm{pc}$. Both our simulated disks included star formation and radiative cooling, with our second model also including a diffuse heating term, representative of the photoelectric heating from dust grains. We did not include any form of localized energetic feedback (e.g. supernovae).

Both the disks fragmented through gravitational instabilities to form a population of clouds, which we identified as GMCs when their densities reached the threshold value of $n_{\mathrm{H,c}} > 100\,\mathrm{cm}^{-3}$. These were tracked over time to provide statistics both as a function of simulation time and of cloud age.

The number of clouds formed above $M_c > 10^5\,\mathrm{M}_\odot$ was found to agree well with the observed Milky Way GMC population. The properties of the clouds were also comparable to observations, including the distributions of cloud mass, size, mass surface density, virial parameter, angular momentum, vertical height above the disk and the distribution of angles of angular momentum with respect to the galactic rotation axis.

Cloud ages were found to lie largely between $0-20\,\mathrm{Myr}$, in good agreement with current estimates. It is notable that this is without a source of localized feedback which has previously been expected to provide a dominant mechanism for cloud destruction. Many of our clouds die in the first 3 Myrs, reducing our population by 50%. This cloud infant mortality is due to mergers with nearby forming clouds and star formation which can destroy low mass ($M < 10^5\,\mathrm{M}_\odot$) objects.

The inclusion of diffuse heating raised the pressure of the warm and cold ISM to suppress the fragmentation of the disk, producing an initially smaller population of clouds embedded in a more massive and structured warm ISM. The denser ISM retains a filamentary structure after fragmentation that maintains a lower velocity dispersion than when heating was absent. This environment has two major impacts on the cloud properties:

1. The filamentary warm ISM produces a predominantly prograde rotating population of clouds even at late times. Without diffuse heating, the clouds become 1/3rd retrograde both with and without star formation. This is evidence that the environment of the cloud plays a dominant role in its evolution.

2. The second effect is that the lower mass of cloud material in the disk reduces the star formation rate in the first 175 Myr of the simulation. Past this time, the star formation rate remained approximately constant, while in the absence of heating, gas depletion in the clouds causes the production of stars to drop by a factor of 10.

Cloud mergers and interactions were a frequent occurrence in both disks, occurring at a rate of ~ 0.25 of an orbital period. This is only slightly higher than the merger rate recorded in TT09 of the same simulation without star formation. The effect of mergers appears to be to reduce the cloud density, thereby reducing the star formation rate, but we note this effect is likely to be dependent on resolution.

The star formation rate in the disks was roughly a factor of 10 too high in both the disk without diffuse heating and when it was included. There are several possibilities why this could be the case including the absence of localized feedback and processes such as added support from magnetic fields. Previous work that explores the impact of magnetic fields on the GMC population suggests that the magnetic pressure can suppress the formation of the population. However, research performed by Dobbs & Price (2008), suggests that the gas to magnetic pressure must be $\beta \lesssim 0.1$ for the magnetic

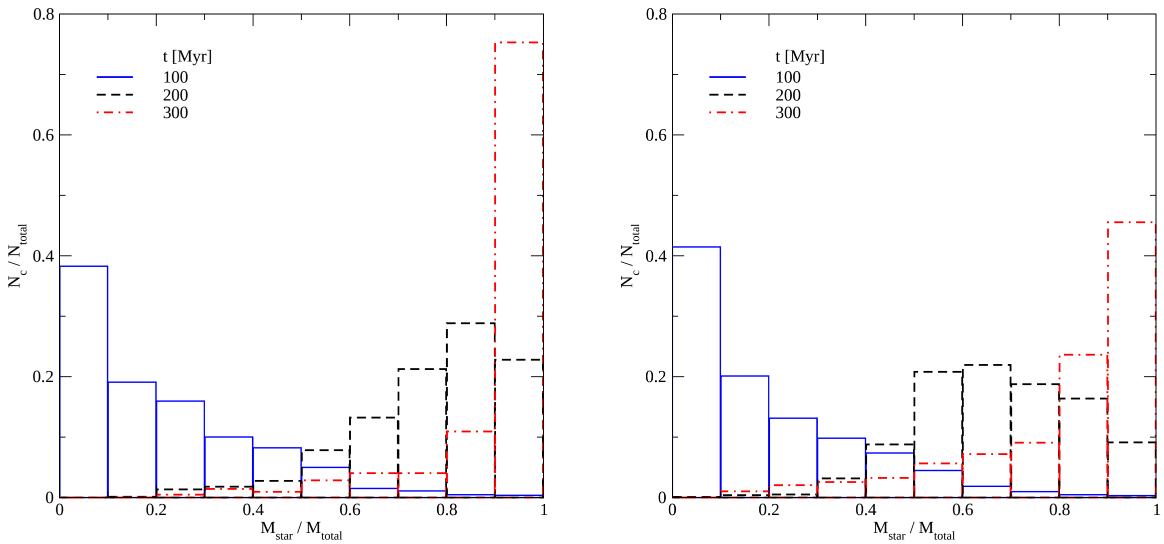

FIG. 16.— Fraction of mass in stars for clouds at simulation times 100 Myr (solid blue line), 200 Myr (dashed black line) and 300 Myr (red dot-dashed line). Left plot shows results for disk SFOnly while the right-hand plot shows the clouds in disk SF+PEheat.

fields to suppress fragmentation in cold gas. Alone, the magnetic Parker instability is not thought to be able to produce a realistic population of GMCs, although it might play a role in seeding the gravitational collapse (Kim & Ostriker 2006). At the other end of the scale, localized feedback from sources such as supernovae or radiation driven winds can destroy clouds once they have formed stars. The exploration of both these mechanisms will be explored in future studies.

In addition to the physical processes not yet included, a second source of error has to be the limit of our resolution. On average, our clouds contain 76 cells and, for an average radius of 16 pc, this equates to roughly 4 cells in each dimension, although it is worth noting that our average radius in the plane of the disk is larger, at 34 pc. The impact this has on our calculations for the cloud properties was investigated in TT09. Figure 11 in that paper shows the effect of reducing our limiting resolution to 15.6 pc and 31.2 pc, plotting the cloud properties shown in Figures 7 and 8 for the populations in these runs. We found that clouds with masses $M \gtrsim 10^6\,\mathrm{M}_\odot$ were converged at all resolutions, but the peak mass, radius and virial parameter decreased with increasing refinement. Of particular concern was the sensitivity of the rotational dynamics of the clouds to resolution. Federrath et al. (2010) find that 30 cells are needed to accurately resolve a vortex, which is almost a factor of ten more than the resolution we are currently able to achieve within our clouds. To test the impact of this, we plotted the variation of the clouds' angular momentum with respect to the disk's rotation in Figure 14 for clouds with masses greater than $M > 10^6\,\mathrm{M}_\odot$, but saw no change in the distribution of θ. This is a promising indication that our result will remain true for a more highly resolved cloud structure, but we note that we are not able to test this directly at the present time.

The author would like to thank Jonathan Tan, Ralph Pudritz and James Wadsley for helpful discussions. EJT also acknowledges the University of Florida High-Performance Computing Center for providing computational resources and support and use of the NCSA Tera-Grid.

REFERENCES

Banerjee, R., Vázquez-Semadeni, E., Hennebelle, P., & Klessen, R. S. 2009, MNRAS, 398, 1082
Bertoldi, F., & McKee, C. F. 1992, ApJ, 395, 140
Bigiel, F., Leroy, A., Walter, F., Brinks, E., de Blok, W. J. G., Madore, B., & Thornley, M. D. 2008, AJ, 136, 2846
Binney, J., & Merrifield, M. 1998, Galactic astronomy, Princeton, NJ : Princeton University Press, 1998
Blitz, L., Bazell, D., & Desert, F. X. 1990, ApJ, 352, L13
Blitz, L., & Rosolowsky, E. 2004, arXiv:astro-ph/0411520
Bolatto, A., D., Leroy, A. K., Rosolowsky, E., Walter, F., Blitz, L. 2008, ApJ, 686, 948
Boulares, A., & Cox, D. P. 1990, ApJ, 365, 544
Bryan,G.L. Comp. Phys. and Eng. 1999, 1:2, p.
Bryan, G. L. & Norman, M. L. 1997, ASP Conf. Ser. 123: Computational Astrophysics; 12th Kingston Meeting on Theoretical Astrophysics, 363
Cox, D. P. 2005, ARA&A, 43, 337
Crutcher, R. M. 2005, in *Massive star birth: A crossroads of Astrophysics*, IAU Symp. 227, ed. by Cesaroni, R., Felli, M., Churchwell, E., Walmsley, M., (Cambridge: CUP), pp.98
Dobbs, C. L. 2008, MNRAS, 391, 844
Dobbs, C. L., & Price, D. J. 2008, MNRAS, 383, 497
Draine, B. T. 1978, ApJS, 36, 595
Federrath, C., Klessen, R. S., & Schmidt, W. 2008, ApJ, 688, L79
Federrath, C., Roman-Duval, J., Klessen, R. S., Schmidt, W., & Mac Low, M.-M. 2010, A&A, 512, A81
Fukui, Y., Kawamura, A., Minamidani, T., Mizuno, Y., Kanai, Y. et al. 2008, ApJS, 178, 56
Fukui, Y., et al. 2009, ApJ, 705, 144
Gammie, C. F., Ostriker, J. P., & Jog, C. J. 1991, ApJ, 378, 565
Genzel, R., et al. 2010, MNRAS, 407, 2091
Glover, S. C. O., & Mac Low, M.-M. 2007, ApJS, 169, 239
Glover, S. C. O., & Mac Low, M.-M. 2007, ApJ, 659, 1317
Glover, S. C. O., Federrath, C., Mac Low, M.-M., & Klessen, R. S. 2010, MNRAS, 404, 2

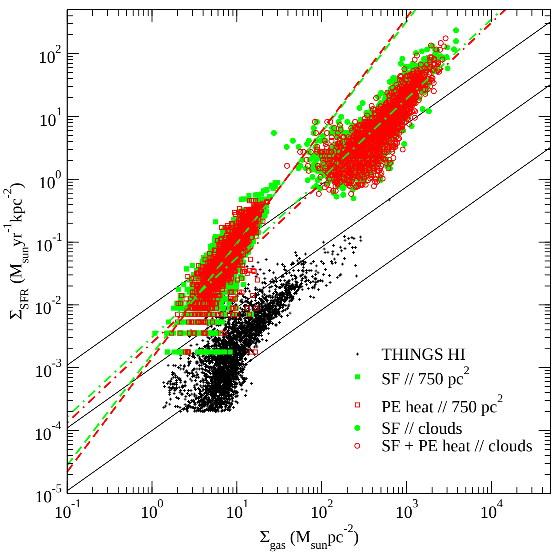

FIG. 17.— The surface SFR, $\Sigma_{\rm sfr}$, vs. surface gas density, $\Sigma_{\rm gas}$ for the cloud populations in our two disks at t = 200 Myr. The surface area is taken to be in the y-z plane, i.e. as if the clouds were viewed from inside the disk. Filled green squares are for an averaged area of 750 pc across around each cloud (equivalent spatial resolution to the observations) in disk SFOnly with a best fit gradient of $\alpha_{\rm sfr} = 1.77$. Open red squares show the same averaged area around clouds in disk SF+PEheat with $\alpha_{\rm sfr} = 1.81$. Filled green circles show the relation averaged over just the cloud's surface area in disk SFOnly, with an $\alpha_{\rm sfr} = 1.27$. Open red circles show the same in disk SF+PEheat and with an $\alpha_{\rm sfr} = 1.27$. Black crosses display the observational results from the THINGS survey (Bigiel et al. 2008). The diagonal solid lines mark constant star formation efficiency, indicating the level of $\Sigma_{\rm SFR}$ required to consume 1%, 10% and 100% of the gas in 10^8 Myr (as shown in Bigiel et al. (2008)). When averaged over the same area as the observations, our SFR is a factor of ~ 10 too high, probably due to the lack of localized feedback. At this resolution, we would expect our gas to be largely atomic, with a steeper gradient similar to that of the observations below $\Sigma_{\rm gas} \lesssim 10\,{\rm M_\odot\,pc^{-2}}$. At the cloud resolution level, the gas should be at least 50% molecular (depending on the size of the atomic envelope) and has a gradient approaching the observations for pure molecular gas, $\Sigma_{\rm gas} \gtrsim 10\,{\rm M_\odot\,pc^{-2}}$.

Habing, H. J. 1968, Bull. Astron. Inst. Netherlands, 19, 421
Heitsch, F., Hartmann, L. W., Slyz, A. D., Devriendt, J. E. G., & Burkert, A. 2008, ApJ, 674, 316
Heitsch, F., Ballesteros-Paredes, J., & Hartmann, L. 2009, ApJ, 704, 1735
Hennebelle, P., Banerjee, R., Vázquez-Semadeni, E., Klessen, R. S., & Audit, E. 2008, A&A, 486, L43
Joung, M. K. R., & Mac Low, M.-M. 2006, ApJ, 653, 1266
Kennicutt, R. C., Jr. 1998, ApJ, 498, 541
Kim, W.-T., & Ostriker, E. C. 2001, ApJ, 559, 70
Kim, W.-T., Ostriker, E. C., & Stone, J. M. 2003, ApJ, 599, 1157
Kim, W.-T., & Ostriker, E. C. 2006, ApJ, 646, 213
Kim, W.-T., & Ostriker, E. C. 2007, ApJ, 660, 1232
Kim, C.-G., Kim, W.-T., & Ostriker, E. C. 2008, ApJ, 681, 1148
Krumholz, M. R., & McKee, C. F. 2005, ApJ, 630, 250
Krumholz, M. R., & Tan, J. C. 2007, ApJ, 654, 304
Kwan, J. 1979, ApJ, 229, 567
Lada, C. J., Lombardi, M., & Alves, J. F. 2010, arXiv:1009.2985
Lada, C. J., & Lada, E. A. 2003, ARA&A, 41, 57
Larson, R. B. 1981, MNRAS, 194, 809
McKee, C. F., & Ostriker, E. C. 2007, ARA&A, 45, 565
McKee, C. F., & Ostriker, J. P. 1977, ApJ, 218, 148
Murray, N., & Rahman, M. 2010, ApJ, 709, 424
Murray, N. 2010, arXiv:1007.3270
O'Shea, B. W., Bryan, G., Bordner, J., Norman, M. L., Abel, T., Harkness, R., & Kritsuk, A. 2004, ArXiv Astrophysics e-prints, astro-ph/0403044
Robertson, B. E., & Kravtsov, A. V. 2008, ApJ, 680, 1083
Rosen, A. & Bregman, J. N. 1995, ApJ, 440, 634
Rosolowsky, E., Engargiola, G., Plambeck, R., & Blitz, L. 2003, ApJ, 599, 258
Sarazin, C. L. & White, R. E. 1987, ApJ, 320, 32
Shetty, R., & Ostriker, E. C. 2006, ApJ, 647, 997
Shetty, R., & Ostriker, E. C. 2008, ApJ, 684, 978
Shetty, R., Glover, S. C., Dullemond, C. P., & Klessen, R. S. 2010, arXiv:1011.2019
Slyz, A. D., Devriendt, J. E. G., Bryan, G., & Silk, J. 2005, MNRAS, 356, 737
Solomon, P. M., Rivolo, A. R., Barrett, J., & Yahil, A. 1987, ApJ, 319, 730
Stark, A. A., & Lee, Y. 2005, ApJ, 619, L159
Stone, J. M. & Norman, M. L. 1992, ApJS, 80, 753
Tan, J. C. 2000, ApJ, 536, 173
Tasker, E. J., & Bryan, G. L. 2006, ApJ, 641, 878
Tasker, E. J., & Bryan, G. L. 2008, ApJ, 673, 810
Tasker, E. J., Brunino, R., Mitchell, N. L., Michielsen, D., Hopton, S., Pearce, F. R., Bryan, G. L., & Theuns, T. 2008, MNRAS, 390, 1267
Tasker, E. J., & Tan, J. C. 2009, ApJ, 700, 358
Tonnesen, S., & Bryan, G. L. 2010, ApJ, 709, 1203
Truelove, J. K., Klein, R. I., McKee, C. F., Holliman, J. H., Howell, L. H., & Greenough, J. A. 1997, ApJ, 489, L179
Toomre, A. 1964, ApJ, 139, 1217
Wada, K., & Norman, C. A. 2007, ApJ, 660, 276
Williams, J. P., & McKee, C. F. 1997, ApJ, 476, 166
Wong, T., & Blitz, L. 2002, ApJ, 569, 157
Wolfire, M. G., Hollenbach, D., McKee, C. F., Tielens, A. G. G. M., & Bakes, E. L. O. 1995, ApJ, 443, 152
Wolfire, M. G., McKee, C. F., Hollenbach, D., & Tielens, A. G. G. M. 2003, ApJ, 587, 278
Zuckerman, B., & Evans, N. J., II 1974, ApJ, 192, L149

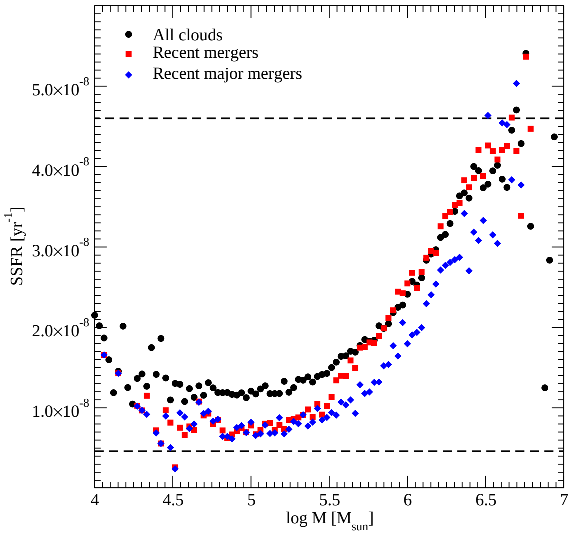

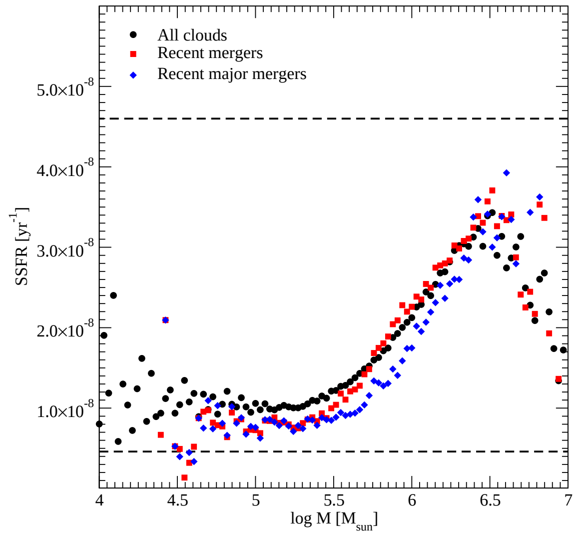

Fig. 18.— Specific star formation rate averaged over one dynamical time (cloud free-fall time) vs. cloud gas mass for individual clouds in disk SFOnly (left plot) and disk SF+PEheat (right). Black circles show the distribution for all clouds, red squares include only clouds that have undergone a merger in the last dynamical time and blue diamonds include only the clouds for whom that merger was with a cloud greater than 50% of its mass.